

LY α EMITTING GALAXIES AS EARLY STAGES IN GALAXY FORMATION^{1,2,3}

LENNOX L. COWIE,⁴ AMY J. BARGER,^{5,6,4} ESTHER M. HU⁴

Draft version June 10, 2018

ABSTRACT

We present optical spectroscopy of two samples of *GALEX* grism selected Ly α emitters (LAEs): one at $z = 0.195 - 0.44$ and the other at $z = 0.65 - 1.25$. We have also observed a comparison sample of galaxies in the same redshift intervals with the same UV magnitude distributions but with no detected Ly α . We use the optical spectroscopy to eliminate active galactic nuclei (AGNs) and to obtain the optical emission-line properties of the samples. We compare the luminosities of the LAEs in the two redshift intervals and show that there is dramatic evolution in the maximum Ly α luminosity over $z = 0 - 1$. Focusing on the $z = 0.195 - 0.44$ samples alone, we show that there are tightly defined relations between all of the galaxy parameters and the rest-frame equivalent width (EW) of H α . The higher EW(H α) sources all have lower metallicities, bluer colors, smaller sizes, and less extinction, consistent with their being in the early stages of the galaxy formation process. We find that $75 \pm 12\%$ of the LAEs have $\text{EW(H}\alpha\text{)} > 100 \text{ \AA}$, and, conversely, that $31 \pm 13\%$ of galaxies with $\text{EW(H}\alpha\text{)} > 100 \text{ \AA}$ are LAEs. We correct the broadband magnitudes for the emission-line contributions and use spectral synthesis fits to estimate the ages of the galaxies. We find a median age of $1.1 \times 10^8 \text{ yr}$ for the LAE sample and $1.4 \times 10^9 \text{ yr}$ for the UV-continuum sample without detected Ly α . The median metallicity of the LAE sample is $12 + \log(\text{O/H}) = 8.24$, or about 0.4 dex lower than the UV-continuum sample.

Subject headings: cosmology: observations — galaxies: distances and redshifts — galaxies: abundances — galaxies: evolution — galaxies: starburst

1. INTRODUCTION

Ly α emission-line searches have been widely used to find high-redshift galaxies and, for the highest redshift galaxies, this line is the only spectroscopic signature that can be used to confirm the redshift of a galaxy selected on the basis of its color properties. However, Ly α is a difficult line to interpret. Because the line is resonantly scattered by neutral hydrogen, determining its escape path and hence its dust destruction is an extremely complex problem, both theoretically (e.g., Neufeld 1991; Finkelstein et al. 2007) and observationally (e.g., Kunth et al. 2003; Schaerer & Verhamme 2008; Östlin et al. 2009). Thus, while we have empirical measurements that a significant fraction of UV-continuum selected samples have Ly α lines with rest-frame equivalent widths above 20 \AA over a wide range of redshifts from $z = 0.3$ to $z = 6.5$ (Shapley et al. 2003; Cowie et al. 2010, 2011; Stark et al. 2010), our understanding of what determines this fraction is still weak. In particular, we would like to know whether the presence of Ly α emission is related to other properties of the galaxy, such as its metallicity, extinction, morphology, or kinematics, and how the Ly α line escapes.

Due to the difficulty with observing in the UV, we currently have much more information on the $z \sim 2 - 3$ Ly α

emitters (LAEs) and how their properties relate to those of other UV selected galaxies at these redshifts (e.g., Shapley et al. 2003; Reddy et al. 2010; Kornei et al. 2010) than we do on the local samples. However, there has been considerable controversy in the interpretation of these high-redshift observations. The simplest interpretation is that the LAEs are younger, lower mass, and metal poor, representing early stages in galaxy evolution (e.g., Hu et al. 1998; Nilsson et al. 2007; Gawiser et al. 2007). However, other authors have argued that LAEs arise in relatively massive galaxies (e.g., Lai et al. 2008; Finkelstein et al. 2009c) with ages of around a Gyr, that young galaxies have weaker Ly α than old galaxies (Shapley et al. 2001), and, more recently, that LAEs are older, less dusty, and in a later stage of galaxy evolution than sources with weaker Ly α emission (Kornei et al. 2010).

The Ly α signature can be produced by a range of galaxy types and masses, including even the most ultraluminous infrared galaxies (ULIRGs) (e.g., Chapman et al. 2005; Nilsson & Møller 2009), so some level of heterogeneity must be expected. However, all of the results that argue for the LAEs being predominantly old are based on spectral synthesis fitting, and most of the old ages inferred are almost certainly mis-estimates arising from the presence

¹Based in part on data obtained from the Multimission Archive at the Space Telescope Science Institute (MAST). STScI is operated by the Association of Universities for Research in Astronomy, Inc., under NASA contract NAS5-26555. Support for MAST for non-HST data is provided by the NASA Office of Space Science via grant NAG5-7584 and by other grants and contracts.

²Based in part on data obtained at the W. M. Keck Observatory, which is operated as a scientific partnership among the the California Institute of Technology, the University of California, and NASA and was made possible by the generous financial support of the W. M. Keck Foundation.

³This research used the facilities of the Canadian Astronomy Data Centre operated by the National Research Council of Canada with the support of the Canadian Space Agency.

⁴Institute for Astronomy, University of Hawaii, 2680 Woodlawn Drive, Honolulu, HI 96822.

⁵Department of Astronomy, University of Wisconsin-Madison, 475 North Charter Street, Madison, WI 53706.

⁶Department of Physics and Astronomy, University of Hawaii, 2505 Correa Road, Honolulu, HI 96822.

of very strong optical emission lines in the LAEs (e.g., Schaerer & deBarros 2009).

Until recently the only low-redshift Ly α emitting sources that could be studied in detail were the local blue compact galaxies. However, these generally have much lower Ly α luminosities than the high-redshift LAEs, and, while some of the blue compact galaxies have been studied in exquisite detail (e.g., Östlin et al. 2009) on an individual basis, it has not been easy to form large, uniformly selected samples that can be statistically analyzed. Thus, the recent determination that substantial $z \sim 0.2 - 0.4$ samples of LAEs can be found (Deharveng et al. 2008) with the *Galaxy Evolution Explorer* (*GALEX*) (Martin et al. 2005) grism spectrographs has enabled a new approach to the subject (Atek et al. 2009a; Finkelstein et al. 2009a, 2009b; Scarlata et al. 2009; Cowie et al. 2010).

The low-redshift LAE samples have many advantages. The galaxies are bright and can be easily studied at other wavelengths, but perhaps even more importantly, they can be integrated into comprehensive studies of galaxies at the same redshifts to understand the selection biases intrinsic to the samples. Early papers on *GALEX* LAEs worked with relatively small samples, but the general conclusions are that low-redshift LAEs are somewhat heterogeneous yet more weighted to low metallicities and extinctions and more likely to be small, compact galaxies when compared to UV-continuum selected galaxies without detected Ly α with the same luminosities in the same redshift interval.

Here we study larger and more optically spectroscopically complete samples of LAEs at $z = 0.195 - 0.44$ and $z = 0.65 - 1.25$, together with comparison samples of UV-continuum selected galaxies without detected Ly α in the same redshift intervals. In Section 2 we present our optical spectroscopy of all the samples obtained with the DEep Imaging Multi-Object Spectrograph (DEIMOS; Faber et al. 2003) on the Keck II 10 m telescope. In Section 3 we use the optical data to remove the small number of active galactic nuclei (AGNs) that were not previously identified from the UV spectra and then provide our final sample of candidate LAE galaxies in the two redshift intervals. We also use the spectra to measure the optical line fluxes and equivalent widths and to determine the metallicities of the galaxies. In Section 4 we determine how the Ly α luminosity evolves with redshift. In Section 5 we consider the overall properties of the LAEs and the UV-continuum selected galaxies without detected Ly α . Since the sample of $z \sim 1$ LAEs is small (only eight objects) we only consider the $z = 0.195 - 0.44$ sample in this section. We use the spectra to determine the emission-line contributions to the broadband fluxes and to show that these corrections must be included if spectral synthesis fitting is to give accurate ages for the youngest ($< 10^9$ yr) galaxies. In Section 6 we interpret the results in terms of a constant star formation rate (SFR) model, comparing SFRs derived from the H α , UV-continuum, and 20 cm observations and discussing the limits of validity for the UV-continuum determined SFRs. We also interpret the metallicity evolution. We summarize our results in Section 7. We use a standard $H_0 = 70 \text{ km s}^{-1} \text{ Mpc}^{-1}$, $\Omega_M = 0.3$, $\Omega_\Lambda = 0.7$ cosmology.

For the present study we use the LAE samples with rest-frame $\text{EW}(\text{Ly}\alpha) > 15 \text{ \AA}$ from Cowie et al. (2010; their Tables 15 and 16), chosen from the nine blank high galactic latitude fields with the deepest *GALEX* grism spectroscopic observations (Morrissey et al. 2007). The area covered is just over 8 deg^2 . The samples consist of sources whose grism UV spectra have a detectable single emission line, which we assume to be Ly α . In order to eliminate sources that are clearly AGNs based on their UV spectra, we do not include any sources that have high-ionization lines, and we require the FWHM of the Ly α lines to be less than 15 \AA in the *GALEX* FUV spectra ($z = 0.195 - 0.44$) or less than 30 \AA in the *GALEX* NUV spectra ($z = 0.65 - 1.25$). In the redshift interval $z = 0.65 - 1.25$ we also eliminate sources that do not show the break between the FUV and NUV bands. Such a break would be expected to be produced by the Lyman continuum edge. (See Section 4 of Cowie et al. 2010 for details on constructing the samples.) For the CDFS 00 field we have added additional sources from a deeper grism spectroscopic exposure than was used in Cowie et al. (2010). The full Ly α selected sample in the CDFS 00 is given in the Appendix (i.e., this is an update of Table 4 in Cowie et al. 2010, but it also includes the optical redshifts, where available; see Section 2.2).

We summarize the final candidate LAE galaxy sample in the redshift interval $z = 0.195 - 0.44$ in Table 1, sorted by the rest-frame $\text{EW}(\text{Ly}\alpha)$. Through most of the paper we restrict our analysis to sources with rest-frame $\text{EW}(\text{Ly}\alpha) \geq 20 \text{ \AA}$, so we list these sources in the main body of the table. However, for completeness, we also give the results for the lower $\text{EW}(\text{Ly}\alpha)$ sources in a supplement to the table. For each source in Table 1 we give the *GALEX* name, the J2000 right ascension and declination, the redshift from the *GALEX* UV spectrum, the logarithm of the bolometric continuum luminosity, $L_\nu\nu$, above 1216 \AA , the logarithm of the Ly α luminosity, the rest-frame $\text{EW}(\text{Ly}\alpha)$, the optical ground-based redshift, the rest-frame $\text{EW}(\text{H}\alpha)$, the $[\text{NII}]\lambda 6584/\text{H}\alpha$, $[\text{OIII}]\lambda 5007/\text{H}\beta$, and $[\text{OIII}]\lambda 4363/\text{H}\gamma$ ratios, and the logarithm of the H α and H β fluxes for the sources with optical continuum magnitudes in the Sloan Digital Sky Survey (SDSS) (see Section 2.1).

We summarize the final candidate LAE galaxy sample in the redshift interval $z = 0.65 - 1.25$ in Table 2, also sorted by the rest-frame $\text{EW}(\text{Ly}\alpha)$. There are 8 sources in this sample. We list the properties of these sources using the same format as in Table 1, except here we give the rest-frame $\text{EW}(\text{H}\beta)$ in place of the rest-frame $\text{EW}(\text{H}\alpha)$, and we do not include the column for the H α and H β fluxes. We also do not split the sample into a main body of the table and a supplement to the table, since there are so few sources. Six of the eight sources satisfy the $\text{EW}(\text{Ly}\alpha) > 20 \text{ \AA}$ criterion.

Although the $z \sim 1$ sample is small, it is important in that it demonstrates the presence of these LAEs, and it allows us to make a first estimate of the luminosity function at these redshifts. However, most of our analysis in this paper will focus on the $z \sim 0.3$ sample. For each source with $z < 0.3$ we computed the UV spectral index from the *GALEX* spectra using the Calzetti et al. (1994) prescription, which fits a power law to the spectrum in a set of wavelength windows chosen to minimize the effects of absorption and emission lines. Since we have only short

wavelength data in the rest frame, we corrected our measured index with the offset of -0.16 given by Meurer et al. (1999) to provide our final index. We did not compute the UV spectral index for the sources with $z > 0.3$, since at those redshifts many of the shortest wavelength windows in Calzetti et al. (1994) lie in the noisy regions between the *GALEX* FUV and NUV spectra.

2.1. Imaging Data

We compiled ancillary data from various archival sources. Just over 82% of the area is covered by deep *U*-band images obtained with the MegaPrime camera on the 3.6 m Canada France Hawaii Telescope (CFHT). We took the reduced images from the CADC pipeline reduction, which gives the 5σ AB magnitude limits. These range from 26.5 to 27.5. We used these images to measure the *U*-band magnitudes and the FWHM sizes of the galaxies at this wavelength. For the fields covered by the SDSS we also compiled the u' , g' , r' , i' , and z' SDSS model C magnitudes (2σ AB magnitude limits of 22.0, 22.2, 22.2, 21.3, and 20.5, respectively) from the DR6 release (Adelman-McCarthy et al. 2008). These cover roughly half of the observed targets. For the fields with publicly available 20 cm images (COSMOS 00: Schinnerer et al. 2007, 1σ of $10.5 \mu\text{Jy beam}^{-1}$; SIRTFFL 01: Condon et al. 2003, 1σ of $23 \mu\text{Jy beam}^{-1}$; HDFN 00: Morrison et al. 2010, 1σ ranges from $3.9 \mu\text{Jy beam}^{-1}$ near the center to $8 \mu\text{Jy beam}^{-1}$ at $15'$), we measured the 20 cm fluxes from the images following the usual methods (e.g., Morrison et al. 2010). Finally, for the CDFS 00 targets covered by the Galaxy Evolution from Morphologies and SEDs (GEMS) survey (Rix et al. 2004), we compiled thumbnails of the galaxies in the F606W (5σ AB magnitude limit of 28.25) and F850LP (5σ AB magnitude limit of 27.10) filters from the *Hubble Space Telescope* (*HST*) observations with the Advanced Camera for Surveys (ACS).

2.2. Optical Spectroscopy

We obtained optical spectroscopy for a large fraction of the two *GALEX* LAE samples using the DEIMOS spectrograph on Keck II with the ZD600 ℓ/mm grating in observing runs throughout 2009 and 2010. The $\sim 0.5 - 1.0$ hr spectra have a resolution of 4.5 \AA and a wavelength range of approximately 5000 \AA centered at 6800 \AA . More details of the observing and reduction procedures can be found in Cowie et al. (1996, 2010).

We observed 77 of the 91 $z = 0.195 - 0.44$ LAEs in Table 1 (this includes the supplement) and all 8 $z = 0.65 - 1.25$ LAEs in Table 2. We give the optical redshifts in Tables 1 and 2, where they can be compared with the UV redshifts from the *GALEX* data. For the 77 $z = 0.195 - 0.44$ LAEs with optical redshifts, we confirmed the UV redshifts for 70. In Table 1 we show the optical redshifts in parentheses for the sources where we did not confirm the UV redshifts. We eliminated these sources from further consideration. We confirmed the UV redshifts for all 8 $z = 0.65 - 1.25$ LAEs with the optical redshifts. We show the UV and optical spectra for these sources in Figures 1 and 2.

In order to understand how the *GALEX* LAEs relate to other UV-continuum selected sources with the same UV-continuum magnitude distributions, we also observed at optical wavelengths sources randomly chosen from the

GALEX UV spectroscopic sample that did not have UV spectral line identifications. The latter is not a complete sample of all such sources in the field, but rather a randomly chosen subsample with an NUV magnitude selection function that is similar to that for the sources with strong $\text{Ly}\alpha$ emission. Thus, it may be directly compared to the LAE sample.

We have obtained optical spectra for 450 of the 5642 objects in the total UV-continuum selected sample without detected $\text{Ly}\alpha$. 114 of these sources lie in the redshift interval $z = 0.195 - 0.44$, and 5 lie in the redshift interval $z = 0.65 - 1.25$. We will hereafter refer to these sources as our *UV-continuum sample*. These sources may be viewed as analogs of high-redshift Lyman break galaxies (LBGs) without strong $\text{Ly}\alpha$ emission and can be combined with the LAE sample to understand how $\text{Ly}\alpha$ galaxies are related to the more general UV-continuum selected population. In order to compare the numbers of UV-continuum sources with a given property with the LAE sample we need to correct for the fraction of UV-continuum sources that were observed. There is a weak dependence of the observed fraction on the NUV magnitude, ranging from 6% observed at $\text{NUV}=20$ to 11% observed at $\text{NUV}=22$. We use the inverse of this fraction as a function of the NUV magnitude to provide the weighting to the UV-continuum sample.

The new optical spectroscopic data presented in this paper more than doubles the optical spectroscopic data used in Cowie et al. (2010). There we observed with DEIMOS (including four literature redshifts) 34 of the 62 $z = 0.195 - 0.44$ LAEs given in their Table 15 (this also includes $\text{EW}(\text{Ly}\alpha) < 20 \text{ \AA}$ sources) and 1 of the 4 $z = 0.65 - 1.25$ LAEs given in their Table 16. We also observed with DEIMOS 124 UV-continuum selected sources without detected $\text{Ly}\alpha$, of which 46 were in the redshift interval $z = 0.195 - 0.44$ and none were in the redshift interval $z = 0.65 - 1.25$.

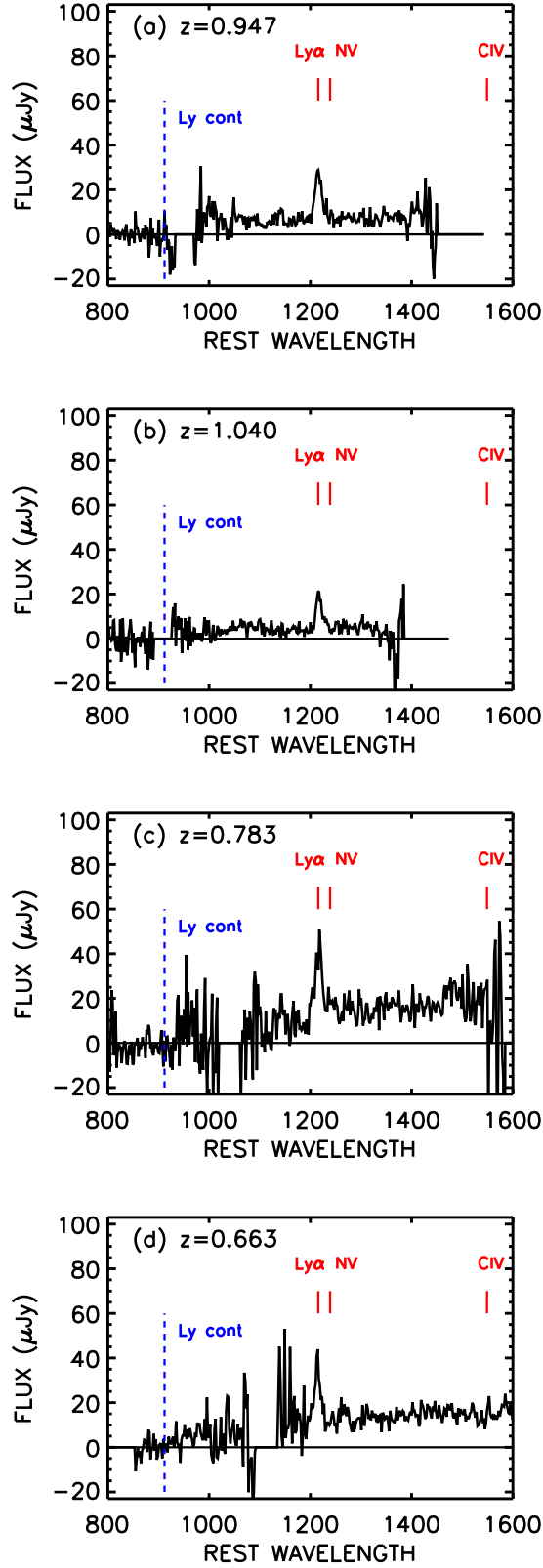


FIG. 1.— *GALEX* spectra of the first four $z = 0.65 - 1.25$ LAEs in Table 2. For each source we give the redshift measured from the UV spectrum. The $\text{Ly}\alpha$ line is marked, as are the positions where CIV and NV would fall. The blue vertical dashed line shows the position of the Lyman continuum edge at the galaxy redshift. This is generally slightly redward of the more accurate optical redshift (see Cowie et al. 2010).

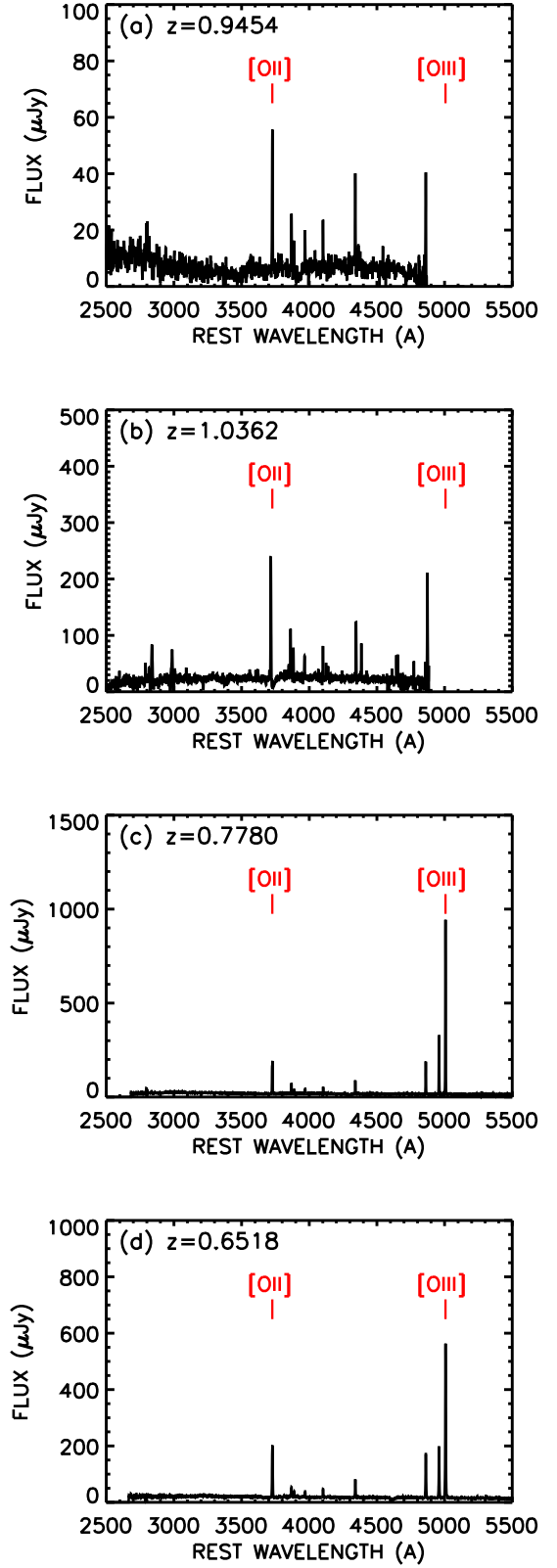


FIG. 2.— *DEIMOS* optical spectra of the first four $z = 0.65 - 1.25$ LAEs in Table 2. For each source we give the redshift measured from the optical spectrum. The positions of the $[\text{OII}]\lambda 3727$ and $[\text{OIII}]\lambda 5007$ lines are marked. Where continuum magnitudes are available we have normalized the spectrum to match these. None was available for the source in (b), so its normalization should be considered to be much more uncertain.

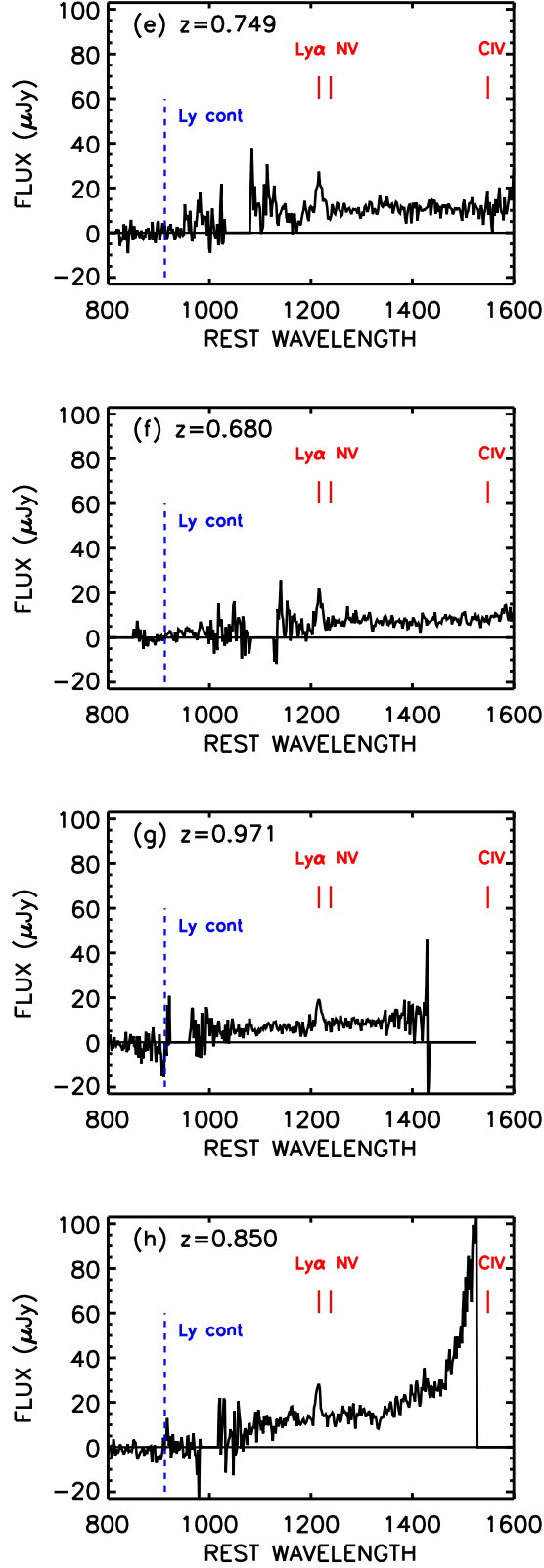


FIG. 1 (CONT).— *GALEX* spectra of the last four $z = 0.65 - 1.25$ LAEs in Table 2. For each source we give the redshift measured from the UV spectrum. The Ly α line is marked, as are the positions where CIV and NV would fall. The blue vertical dashed line shows the position of the Lyman continuum edge at the galaxy redshift. This is generally slightly redward of the more accurate optical redshift (see Cowie et al. 2010).

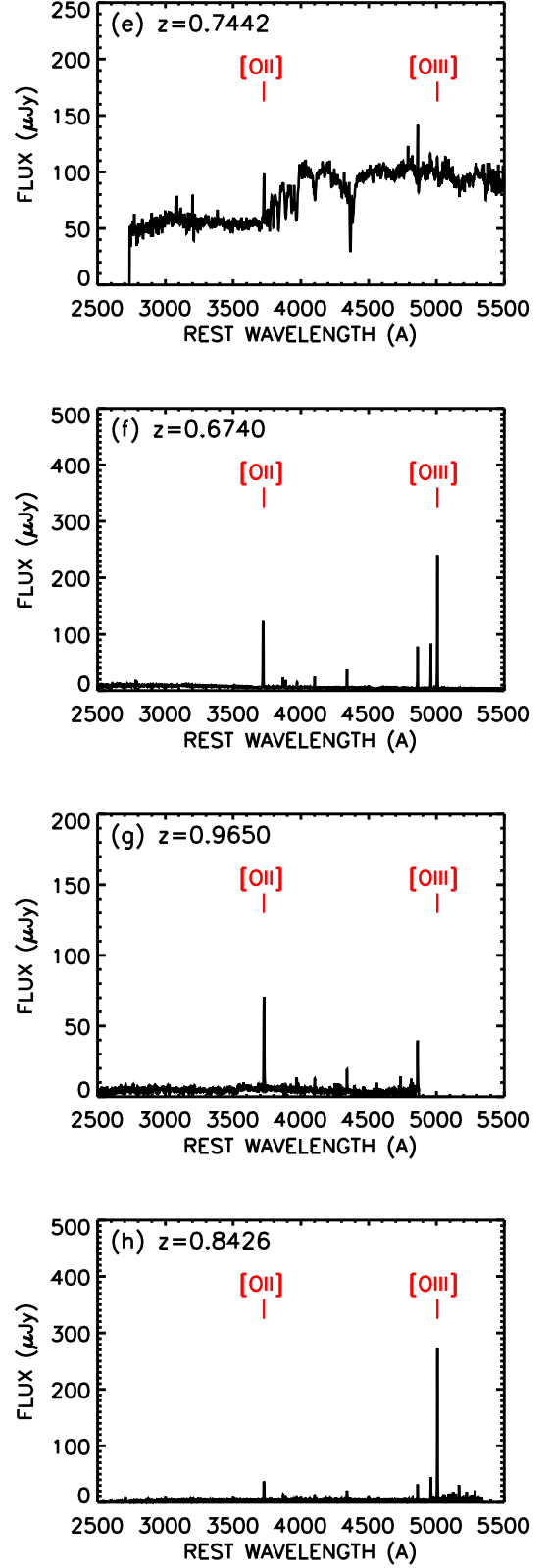


FIG. 2 (CONT).— DEIMOS optical spectra of the last four $z = 0.65 - 1.25$ LAEs in Table 2. For each source we give the redshift measured from the optical spectrum. The positions of the [OII] $\lambda 3727$ and [OIII] $\lambda 5007$ lines are marked. Where continuum magnitudes are available we have normalized the spectrum to match these. None was available for the source in (f), so its normalization should be considered to be much more uncertain.

2.3. Line Fluxes

Most of the spectra were obtained at a near-parallactic angle to minimize atmospheric refraction effects. However, in some cases the mask configuration did not allow for this. In addition, a small number of the spectra were obtained during periods of varying extinction. All of the spectra were relatively calibrated using the measured response from observed calibration stars. However, relative slit losses always pose a problem, and special care must be taken for the flux calibration.

For each spectrum we fitted all of the emission lines using the IDL MPFIT program of Markwardt (2009). We used simultaneous Gaussian fits to neighboring lines together with a linear fit to the continuum baseline. For weaker lines we held the full width constant, using the value measured in the stronger lines, and set the central wavelength to the measured redshift. We also measured the noise as a function of wavelength by fitting to random positions in neighboring portions of the spectrum and computing the dispersion in the results.

For the AGN classifications and the metallicity measurements we used only the ratios of the emission lines that are close in wavelength. These line flux ratios can be robustly measured from the spectra without even the relative flux calibration, since for these neighboring lines the DEIMOS response is essentially constant. For the primary lines used in our analysis we give the line ratios and their 1σ errors in Tables 1 and 2.

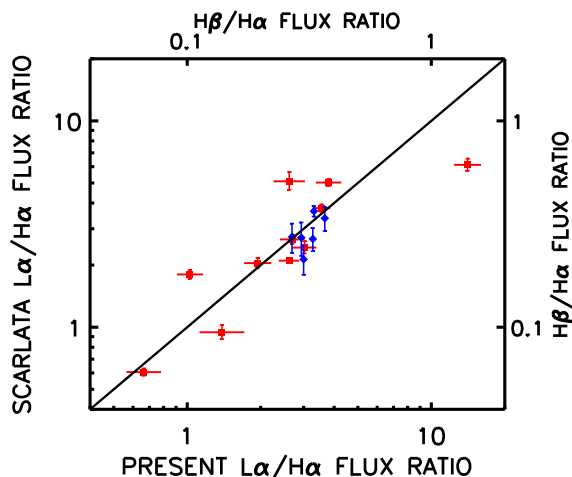


FIG. 3.— Comparison of the $f(\text{Ly}\alpha)/f(\text{H}\alpha)$ ratios (red squares) and the $f(\text{H}\beta)/f(\text{H}\alpha)$ ratios (blue diamonds) measured from the present data with the ratios measured by Scarlata et al. (2009). The scale for the $f(\text{Ly}\alpha)/f(\text{H}\alpha)$ ratios is shown on the bottom and left axes and that for the $f(\text{H}\beta)/f(\text{H}\alpha)$ ratios on the right and top axes. For the $f(\text{Ly}\alpha)/f(\text{H}\alpha)$ ratios the vertical error bars only include the uncertainties in $f(\text{H}\alpha)$, since the uncertainties in $f(\text{Ly}\alpha)$ are not given in Scarlata et al.’s table.

In order to measure the absolute $\text{H}\alpha$ and $\text{H}\beta$ line fluxes, we used the measured $\text{EW}(\text{H}\alpha)$ and $\text{EW}(\text{H}\beta)$ in combination with the measured continuum fluxes at the appropriate wavelength. We first determined which SDSS filter the emission line lay in and then integrated through the transmission of this filter to obtain the averaged spectral flux. We then renormalized the spectrum to match the corresponding SDSS model C magnitude from the DR6 release (Adelman-McCarthy et al. 2008). We then determined the continuum flux and multiplied this by the observed-frame

EW to obtain the corresponding line flux. This is an approximation, since it assumes that the measured EW is representative of the value averaged over the total light of the galaxy, including regions outside the slit. However, for the photometric cases we derive very similar values directly from the calibrated spectra, including calibrated spectra that we obtained using larger ($2''$) slit widths for a small subset of the galaxies. This suggests the procedure is relatively robust.

However, the relative apertures used in measuring the *GALEX* $\text{Ly}\alpha$ fluxes and the optical emission line fluxes may introduce systematic variations reflecting the relative geometries of the emission. Thus, the $f(\text{Ly}\alpha)/f(\text{H}\alpha)$ ratios are more reliably obtained in large ($5''$) aperture measurements, such as those used in Atek et al. (2009a). In the present paper we are primarily concerned with determining the optical continuum and emission-line properties that result in a galaxy showing a strong $\text{Ly}\alpha$ emission line and not so much with the relative fluxes of the optical and $\text{Ly}\alpha$ emission lines, making this less of a concern. In the discussion we will note where aperture effects might play a role.

In order to check the calibrations and aperture effects, we tested our measured fluxes against the independent measurements by Scarlata et al. (2009) for the subset of galaxies that overlap with our sample. The Scarlata et al. data were obtained with a larger $1''.5$ slit. For eight cases they compared their results with those made in a $5''$ slit, finding only small differences between the two measurements. Scarlata et al.’s procedure for measuring the fluxes relied on the relative accuracy of the spectrophotometry, using the i' magnitude from the SDSS data to set the absolute flux normalization. This differs from our procedure, where we normalized each region of the spectrum separately to the SDSS magnitudes. We compare the two results in Figure 3, where we show both the $f(\text{Ly}\alpha)/f(\text{H}\alpha)$ (red squares) and the $f(\text{H}\beta)/f(\text{H}\alpha)$ ratios (blue diamonds). The overall agreement is very good, but in a small number of cases the disagreement is much larger than the statistical error in the $f(\text{Ly}\alpha)/f(\text{H}\alpha)$ ratio. In the most extreme case the ratios differ by a multiplicative factor of just over two. We take this to be an estimate of the potential systematic errors.

3. AGN-GALAXY DISCRIMINATION

We might expect that sources classified as AGNs based on the presence of high-excitation lines or very wide lines in the UV spectra are truly AGNs. However, the converse is not true, which means our candidate LAE galaxies (Tables 1 and 2) may still have some degree of AGN contamination. In some cases the high-excitation lines fall at problematic wavelengths in the UV spectra, and in other cases these lines may be intrinsically weak. Optical spectroscopic data support these points: follow-ups of *GALEX* candidate LAE galaxy samples have shown that a significant fraction ($\sim 20\%$) have substantial AGN contributions (Finkelstein et al. 2009b; Scarlata et al. 2009; Cowie et al. 2010), though there is wide variation in the estimates of the precise degree of contamination reflecting the relatively small sample sizes and the differences in the classification procedures. (Finkelstein et al. 2009b find a higher AGN fraction in their sample than other groups, so we make a detailed comparison with their results in this section.)

TABLE 1
 $z = 0.195 - 0.44$ LAE SAMPLE

NAME	R.A. (J2000.0)	Decl. (J2000.0)	z_{galex}	$\log L_{\nu\nu}$ (erg/s)	$\log L_{\alpha}$ (erg/s)	EW Ly α (Å)	z_{opt}^1	EW H α (Å)	[NII]/H α 6584/6563	[OIII]/H β 5007/4861	[OIII]/H γ 4363/4341	$\log f_{\text{H}\alpha}, f_{\text{H}\beta}$ (erg/cm ² /s)
(1)	(2)	(3)	(4)	(5)	(6)	(7)	(8)	(9)	(10)	(11)	(12)	(13)
GALEX0332-2748	53.221958	-27.809139	0.2277	43.14	42.17	148±12	0.2265	317±2.	0.047±0.004	5.64±0.007	0.101±0.016	... , ...
GALEX1718+5949	259.748260	59.825752	0.3717	43.70	42.24	114±49	(0.5416) , ...
GALEX1417+5228	214.430923	52.468307	0.2104	43.01	42.01	100±9.	0.2083	110±2.	.001±0.001	7.17±0.004	0.468±0.017	-14.6, -15.1
GALEX0333-2733	53.340416	-27.560862	0.2767	43.22	42.08	99±9	0.2758	315±2.	0.049±0.006	5.81±0.049	0.105±0.044	... , ...
GALEX0332-2747	53.195126	-27.787361	0.2277	42.90	41.86	90±11	0.2266	300±2.	0.023±0.005	5.18±0.057	0.275±0.073	... , ...
GALEX1436+3525	219.193008	35.417641	0.3697	43.71	42.32	88±20	0.3681(Sy1.8) , ...
GALEX0331-2814	52.976501	-28.238640	0.2824	43.44	42.18	72±5	0.2803	25±.5	0.561±0.012	0.794±0.041 , ...
GALEX0333-2757	53.496414	-27.966471	0.3630	43.66	42.21	71±12	0.3578(B)	26±1.	0.956±0.015	5.87± 0.11	0.417± 0.37	... , ...
GALEX1422+5252	215.533752	52.873722	0.3055	43.34	42.01	71±8	0.3016(Sy1.5) , ...
GALEX0332-2801	53.049751	-28.025057	0.2191	43.13	41.87	69±6	0.2155	387±1.	0.059±0.002	4.57±0.005	0.018±0.016	... , ...
GALEX1240+6233	190.041428	62.561668	0.2104	43.34	42.01	60±10	0.2068(B)	133±1.	0.255±0.008	7.52±0.012	0.186±0.058	-13.9, -14.5
GALEX0332-2810	53.001919	-28.182611	0.2795	43.12	41.76	55±9	0.2775	110±3.	0.071±0.028	3.04± 0.14	0.480± 0.41	... , ...
GALEX1418+5307	214.728928	53.130028	0.2047	43.02	41.73	53±5	0.2034	301±2.	0.012±0.007	5.59±0.020	0.143±0.092	-14.9, -15.5
GALEX1438+3457	219.746078	34.960636	0.3740	43.79	42.27	50±12	0.3690(B)	6±1.	0.419±0.068	-15.3, ...
GALEX1421+5249	215.463165	52.830891	0.2018	42.95	41.50	49±9	0.2021(Sy1.5) , ...
GALEX0332-2811	53.174255	-28.190306	0.2076	43.74	42.36	48±1	0.2043	334±1.	0.017±0.001	6.47±0.003	0.146±0.011	... , ...
GALEX1419+5315	214.794739	53.265835	0.2651	43.37	41.85	48±6	0.2637	11±1.	0.403±0.035	1.84± 0.31	...	-14.4, -15.3
GALEX1435+3449	218.764587	34.821220	0.3782	43.72	42.03	46±17	(0.4984) , ...
GALEX0332-2722	53.045292	-27.378277	0.3083	43.49	41.94	45±5 , ...
GALEX1001+0220	150.294785	2.346944	0.2508	43.50	42.05	45±3	0.2481	462±2.	0.025±0.004	6.44±0.040	0.190±0.027	-14.5, -15.0
GALEX1000+0157	150.116043	1.951000	0.2680	43.80	42.42	43±2	0.2647	423±1.	0.024±0.002	5.61±0.042	0.171±0.022	-14.1, -14.7
GALEX0334-2815	53.541294	-28.255499	0.3430	43.41	41.83	41±11	0.3370(A)	.7±.5 , ...
GALEX1436+3459	219.100540	34.993530	0.2148	43.27	41.73	40±5	0.2131	60±1.	0.121±0.018	3.76± 0.13	0.687± 0.34	-15.5, ...
GALEX0334-2752	53.711498	-27.876585	0.3371	43.54	42.11	39±5	0.3336(B)	6±1.	0.655± 0.14	1.72± 0.31 , ...
GALEX1714+5949	258.591766	59.833332	0.2306	43.34	41.94	38±5	0.2298	85±1.	0.071±0.010	3.91±0.053	...	-14.8, -15.4
GALEX0330-2744	52.574123	-27.741528	0.2623	43.02	41.52	36±7 , ...
GALEX0332-2809	53.025002	-28.161083	0.2219	42.98	41.30	35±9	0.2148(A)	0±.5	0.527± 0.25	... , ...
GALEX0333-2756	53.389545	-27.946222	0.4293	43.91	42.31	34±7 , ...
GALEX1418+5259	214.733200	52.992195	0.2882	43.38	41.80	34±4	0.2871	150±2.	0.092±0.009	3.79±0.033	0.082±0.039	-14.5, -15.2
GALEX0332-2823	53.240459	-28.388306	0.2191	43.45	41.87	34±3	0.2136	64±.5	0.396±0.005	1.10±0.027 , ...
GALEX0331-2817	52.869667	-28.283443	0.2162	42.96	41.26	33±9	0.2149(A)	2±.5	0.431± 0.13 , ...
GALEX0038-4352	9.520541	-43.874584	0.2220	43.46	41.89	32±3	0.2190	12±1.	0.499±0.037	1.77± 0.29 , ...
GALEX1417+5246	214.438126	52.771694	0.2479	43.15	41.57	32±5	0.2441	146±2.	0.068±0.009	3.74±0.042	0.125±0.069	-15.0, -15.6
GALEX1001+0233	150.413208	2.563583	0.3889	43.87	42.42	32±5	0.3824	313±1.	0.026±0.004	5.41±0.019	0.155±0.011	-14.4, -14.9
GALEX1437+3445	219.334000	34.757637	0.3285	43.74	42.23	31±3	0.3237	137±1.	0.095±0.006	3.50±0.026	0.118±0.025	-14.8, -15.2
GALEX1436+3440	219.086914	34.672001	0.3740	43.93	42.08	29±9	(0.3311) , ...
GALEX1437+3441	219.356308	34.685585	0.2944	43.74	41.96	28±5	0.2900(A)	.7±.5	0.752± 0.25 , ...
GALEX1436+3456	219.092041	34.942139	0.2716	43.62	41.91	27±3	0.2684	67±2.	0.156±0.038	2.52± 0.11	...	-14.8, -15.3
GALEX0331-2814	52.978458	-28.235861	0.3198	43.72	41.89	27±3	0.3163	66±1.	0.411±0.008	0.386±0.020	0.063±0.053	... , ...
GALEX0332-2758	53.102917	-27.977055	0.3803	43.70	41.93	26±7	(0.1231) , ...
GALEX1418+5218	214.593506	52.306747	0.2392	43.19	41.44	26±4	0.2388	170±2.	0.038±0.012	4.41±0.064	0.213± 0.14	-14.8, -15.3
GALEX0332-2811	53.061584	-28.186527	0.2651	43.42	41.72	25±3	0.2611(B)	.7±.5	1.87± 0.20 , ...
GALEX1417+5305	214.291290	53.086723	0.2680	43.45	41.65	25±3	0.2671	42±1.	0.261±0.019	1.16±0.039	...	-15.0, -15.5
GALEX0331-2811	52.962204	-28.188999	0.2162	43.52	41.82	25±2	0.2130(B)	2±.5	0.858± 0.14 , ...
GALEX0334-2743	53.711334	-27.729334	0.3227	43.90	42.09	24±3 , ...
GALEX0959+0149	149.873795	1.832889	0.2076	43.05	41.27	24±6	0.2051	25±.5	0.358±0.010	0.636±0.055	...	-14.9, -15.5
GALEX1434+3532	218.718338	35.547527	0.1977	43.13	41.45	24±5	0.1946	238±2.	0.051±0.005	4.25±0.015	...	-14.6, -15.2
GALEX0334-2803	53.586754	-28.065695	0.3602	43.73	41.95	24±5 , ...
GALEX0332-2810	53.155334	-28.177500	0.2076	43.30	41.58	24±3	0.2035	17±.5	0.355±0.015	0.972±0.095 , ...
GALEX0330-2816	52.737499	-28.279444	0.2853	43.53	41.89	24±2	0.2813	233±1.	0.151±0.004	1.81±0.018 , ...
GALEX0332-2750	53.102707	-27.847721	0.3803	43.67	41.92	23±6	(STAR) , ...
GALEX1423+5246	215.775833	52.779697	0.3458	43.56	41.86	22±4	0.3431	595±1.	0.040±0.003	5.94±0.020	0.135±0.018	-14.3, -14.9
GALEX1421+5239	215.352737	52.655472	0.2565	43.16	41.48	22±3	0.2594	33±1.	0.109±0.029	2.21±0.076	...	-13.9, -15.1
GALEX0959+0151	149.918091	1.855917	0.2536	43.46	41.77	21±3	0.2506	811±2.	0.051±0.001	6.04±0.034	0.096±0.008	-13.9, -14.6
GALEX1420+5306	215.170456	53.114002	0.1989	43.12	41.32	21±4	0.1990(A)	2±78	-15.0, -14.7
GALEX1714+5956	258.683746	59.947247	0.2220	43.28	41.53	21±5	0.2157	27±1.	0.100±0.032	5.08±0.038	...	-15.2, -15.2
GALEX1420+5247	215.132080	52.799389	0.2565	43.60	41.83	20±2	0.2525	72±13	...	9.41± 0.78 , ...
GALEX1725+5920	261.344940	59.345528	0.3861	44.28	42.43	20±6	(.03086) , ...
GALEX0331-2820	52.897709	-28.345751	0.2651	43.29	41.48	20±4 , ...
GALEX0334-2752	53.554749	-27.880083	0.2364	43.25	41.52	20±3	0.2333	300±2.	0.030±0.005	5.45±0.052 , ...
GALEX1717+5944	259.465027	59.748554	0.1960	43.24	41.40	20±6	0.1979	112±1.	0.172±0.010	1.68±0.037	0.094±0.058	-14.4, -15.1

¹The optical redshift is shown in parentheses when it does not agree with the *GALEX* redshift. Intermediate-type Seyferts are labeled as Sy1.5 or Sy1.8, while AGNs identified in the BPT diagram are labeled as B. Galaxies with weak optical emission lines are labeled as A.

TABLE 1
 $z = 0.195 - 0.44$ LAE SAMPLE (SUPPLEMENT)

NAME	R.A. (J2000.0)	Decl. (J2000.0)	z_{galax}	$\log L_{\nu\nu}$ (erg/s)	$\log L_{\alpha}$ (erg/s)	EW Ly α (Å)	z_{opt}^1	EW H α (Å)	[NII]/H α 6584/6563	[OIII]/H β 5007/4861	[OIII]/H γ 4363/4341	$\log f$ $f(\text{H}\alpha), f(\text{H}\beta)$ (erg/cm ² /s)
(1)	(2)	(3)	(4)	(5)	(6)	(7)	(8)	(9)	(10)	(11)	(12)	(13)
GALEX1001+0145	150.396500	1.756222	0.2191	43.14	41.40	19±4	0.2192	68±1.	0.061±0.014	2.54±0.083	...	-15.2, -15.8
GALEX1423+5244	215.842850	52.742474	0.2795	43.29	41.46	19±5	0.2771	39±2.	0.297±0.037	0.853±0.11	...	-15.1, -15.6
GALEX0331-2724	52.949291	-27.402834	0.3688	43.82	41.80	19±5
GALEX0334-2748	53.729584	-27.800833	0.3141	44.20	42.34	19±1
GALEX1421+5224	215.477295	52.406723	0.3515	44.05	42.12	19±2	0.3454	26±5.	0.558±0.011	0.326±0.068	0.421±0.17	-14.2, -14.9
GALEX1716+5932	259.178070	59.548889	0.3600	43.76	41.99	19±6
GALEX1000+0201	150.149017	2.020417	0.2709	43.84	41.99	19±2	0.2653	195±5.	0.060±0.001	4.71±0.031	0.119±0.026	-14.3, -14.9
GALEX1419+5221	214.970749	52.350250	0.2680	43.46	41.57	19±3	0.2647(B)	3.±5.	0.571±0.088	-15.4, ...
GALEX1418+5245	214.521545	52.752110	0.2450	43.51	41.60	19±2	0.2445	285±2.	0.031±0.005	5.82±0.039	0.113±0.046	-14.4, -15.0
GALEX1419+5223	214.811249	52.390808	0.2565	43.14	41.35	19±4	0.2541(A)	76±5.	0.159±0.067	3.37±0.69	...	-14.1, -14.7
GALEX0333-2820	53.286755	-28.333389	0.3697	43.65	41.80	19±6
GALEX1418+5217	214.701202	52.299168	0.2421	43.31	41.42	18±4	0.2398	46±2.	0.062±0.033	3.80±0.22	...	-15.1, -15.9
GALEX0330-2801	52.551250	-28.025417	0.2479	43.21	41.47	18±3
GALEX0330-2801	52.550297	-28.028778	0.2479	43.21	41.38	18±3
GALEX1418+5249	214.732056	52.824558	0.2680	43.43	41.48	18±3	0.2634(B)	1.±5.	1.44±0.25	-15.6, ...
GALEX0333-2801	53.301208	-28.022917	0.2911	43.31	41.52	17±4
GALEX1717+5929	259.379578	59.487473	0.2997	43.91	41.99	17±3	0.2988	34±1.	0.423±0.024	1.09±0.10	...	-14.3, -15.0
GALEX1436+3527	219.026245	35.458553	0.2517	43.65	41.79	17±2	0.2495	74±2.	0.103±0.016	2.53±0.066	...	-14.9, -15.4
GALEX1420+5243	215.180359	52.718750	0.2508	43.45	41.63	17±2	0.2470	70±2.	...	4.83±0.10	...	-15.1, -15.6
GALEX0332-2744	53.080002	-27.745890	0.2191	43.26	41.38	17±3	0.2174	101±1.	0.086±0.006	2.95±0.053	0.115±0.060	...
GALEX0331-2809	52.999332	-28.164444	0.2392	43.46	41.62	17±2	0.2363	188±1.	0.146±0.004	2.57±0.025	0.048±0.036	...
GALEX1420+5250	215.186218	52.835056	0.2536	43.39	41.58	17±2	0.2519	66±2.	0.168±0.038	2.38±0.11	...	-14.8, -15.1
GALEX0331-2809	52.999332	-28.164444	0.2392	43.46	41.62	17±2	0.2363	188±1.	0.146±0.004	2.57±0.025	0.048±0.036	...
GALEX1420+5250	215.186218	52.835056	0.2536	43.39	41.58	17±2	0.2519	66±2.	0.168±0.038	2.38±0.11	...	-14.8, -15.1
GALEX0331-2742	52.755127	-27.715334	0.3141	43.58	41.76	17±2	0.3107	75±1.	0.135±0.009	2.65±0.028	0.091±0.045	...
GALEX0333-2821	53.258461	-28.357668	0.2507	43.62	41.71	17±2	0.2471	76±1.	0.126±0.009	2.50±0.052
GALEX1422+5310	215.500092	53.168472	0.2392	43.10	41.17	16±5	0.2342(A)	16±1.	0.410±0.043	2.10±0.69	...	-15.2, ...
GALEX0333-2814	53.471249	-28.248138	0.2018	43.36	41.45	16±3
GALEX1419+5230	214.907211	52.507057	0.2853	43.41	41.55	15±3	0.2814(A)	10±1.	0.490±0.088	-15.3, -15.8
GALEX0331-2748	52.800335	-27.800335	0.2594	43.19	41.30	15±3	0.2581	98±1.	0.133±0.010	2.32±0.035
GALEX0331-2753	52.850460	-27.894693	0.2594	43.30	41.35	15±3	(STAR)
GALEX1436+3535	219.243362	35.597694	0.2077	43.36	41.40	15±3	0.2055	14±1.	0.453±0.029	0.531±0.16	...	-14.4, -15.1

¹The optical redshift is shown in parentheses when it does not agree with the *GALEX* redshift. Intermediate-type Seyferts are labeled as Sy1.5 or Sy1.8, while AGNs identified in the BPT diagram are labeled as B. Galaxies with weak optical emission lines are labeled as A.

TABLE 2
 $z = 0.65 - 1.25$ LAE SAMPLE

NAME	R.A. (J2000.0)	Decl. (J2000.0)	z_{galax}	$\log L_{\nu\nu}$ (erg/s)	$\log L_{\alpha}$ (erg/s)	EW Ly α (Å)	z_{opt}^1	EW H β (Å)	[NII]/H α 6584/6563	[OIII]/H β 5007/4861	[OIII]/H γ 4363/4341
(1)	(2)	(3)	(4)	(5)	(6)	(7)	(8)	(9)	(10)	(11)	(12)
GALEX1421+5221	215.421539	52.359886	0.9475	44.60	43.21	52±4	0.9454	0.26±0.06
GALEX0334-2753	53.623749	-27.893917	1.0396	44.47	43.08	48±5	1.0362	0.08±0.04
GALEX1712+6001	258.197723	60.022778	0.7830	44.76	43.19	37±4	0.7780	62	...	5.58±0.021	0.10±0.05
GALEX1437+3541	219.281967	35.692280	0.6630	44.54	42.91	29±5	0.6518	64	...	3.50±0.031	0.05±0.02
GALEX1420+5313	215.237045	53.218750	0.7488	44.53	42.84	27±3	0.7442(A)	6	...	0.484±0.16	...
GALEX0331-2737	52.765331	-27.621777	0.6797	44.30	42.53	22±4	0.6740	102	0.03±0.01
GALEX0332-2734	53.084042	-27.573084	0.9705	44.72	42.82	18±2	0.9650	0.10±0.03
GALEX0331-2754	52.854668	-27.916639	0.8945	44.93	42.77	12±2	0.8425	63	0.09±0.06

¹ Galaxies with weak optical emission lines are labeled as A.

We first searched our samples for optical spectra that showed broad emission lines. None of the spectra are quasars or Seyfert 1s, a consequence of this class of source being easily picked out with the UV spectra (Barger & Cowie 2010). However, three of the sources in the $z = 0.195 - 0.44$ sample are intermediate-type Seyferts. In the optical redshift column (col. 8) of Table 1 we have labeled these sources as Sy1.5 or Sy1.8. We eliminate these sources from further consideration.

We next constructed the BPT diagram (Baldwin et al. 1981) for the $z = 0.195 - 0.44$ sample. This diagram uses the $[\text{NII}]\lambda 6584/\text{H}\alpha$ and the $[\text{OIII}]\lambda 5007/\text{H}\beta$ ratios to separate AGNs from star-forming galaxies. $\text{H}\alpha$ is off the spectra in the $z = 0.65 - 1.25$ sample, and we cannot run this test there. In addition, only sources with strong optical emission lines can be classified in this way. We restricted to galaxies that had either $[\text{NII}]\lambda 6584$ or $\text{H}\alpha$ detected with a signal-to-noise above 5 and either $[\text{OIII}]\lambda 5007$ or $\text{H}\beta$ detected with a signal-to-noise above 5.

The BPT diagrams for the (a) LAE and (b) UV-continuum samples having strong optical emission lines defined in this way are shown in Figures 4(a) and 4(b), respectively. The dotted curve traces the Kewley et al. (2001) division between galaxies whose extreme UV ionizing radiation field is dominated by an AGN ($> 50\%$) and those dominated by star formation. It is a theoretical curve based on photoionization models for giant HII regions and a range of stellar population synthesis codes. The dashed curve traces the Kauffmann et al. (2003) division between AGNs and star formers based on an empirical separation of SDSS galaxies. As mentioned above, we have eliminated the intermediate-type Seyferts in Table 1 from Figure 4(a), but the BPT diagram suggests that a further four sources are also AGNs. We mark these with open black squares in Figure 4(a) and label them as “B” in the optical redshift column (col. 8) of Table 1. Another four sources have weak $[\text{OIII}]$ and $\text{H}\beta$ and do not appear on the diagram, but they have strong $\log([\text{NII}]\lambda 6584/\text{H}\alpha) > -0.25$ ratios, which suggests that they are also AGNs. We also label these sources as “B” in column 8 of Table 1. Most of the remaining sources in Figure 4(a) clearly lie along the star-forming galaxy track, as do all the UV-continuum sources in Figure 4(b), though there are a small number of sources that lie in positions where they may have mixed star formation and AGN contributions. None of the results in the paper are changed if we exclude these objects.

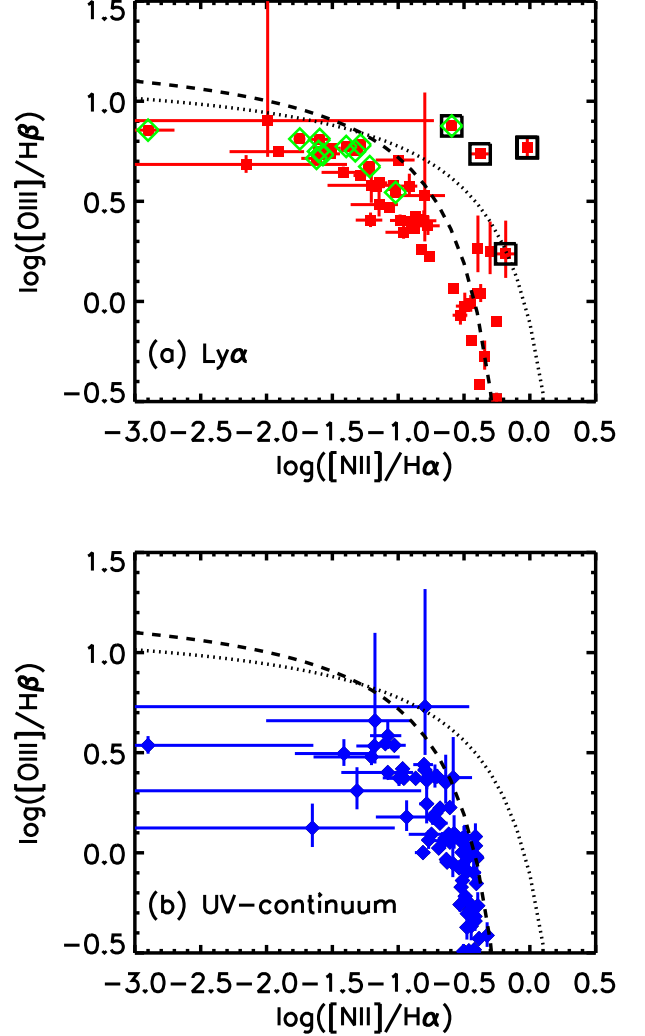


FIG. 4.— (a) BPT diagram for the candidate LAE galaxy sample (Table 1; red solid squares). Sources from both the main table and the supplement (the latter contains sources with rest-frame $\text{EW}(\text{Ly}\alpha)$ between 15 and 20 Å) are included. Only the 58 sources with strong optical emission lines (as defined in the text) are shown. The intermediate-type Seyferts in Table 1 are excluded. The black open squares enclose the sources that we classify as AGNs on the basis of this diagram. (b) BPT diagram for the sources in the UV-continuum sample (blue solid diamonds). Again, only the 82 sources with strong optical emission lines are shown. In both panels the green diamonds show sources where the $[\text{OIII}]\lambda 4363$ auroral line is detected above the 3σ level, the dashed curve denotes the Kauffmann et al. (2003) empirical division between AGNs (upper right) and star-forming galaxies (lower left), and the dotted curve denotes the Kewley et al. (2001) theoretical division.

There remain 8 sources with optical spectra in the LAE sample where the $[\text{OIII}]\lambda 5007$ and $\text{H}\beta$ lines are too weak to place them on the BPT diagram and where the $[\text{NII}]\lambda 6584/\text{H}\alpha$ ratios are not high. These galaxies are labeled as “A” in the optical redshift column (col. 8) of Table 1 for their weak optical emission lines. In one case the optical spectrum is poor, but in the remaining cases the sources either have more normal $[\text{NII}]\lambda 6584/\text{H}\alpha$ ratios or are absorbers. It is possible that these also contain AGNs. The percentage of AGNs in the sample is $16 \pm 4\%$ if we include only the classified AGNs, but that percentage would rise to $27 \pm 6\%$ if the 8 weak emission-line sources

were also AGNs.

Finkelstein et al. (2009b) optically classified 23 sources from the Deharveng et al. (2008) sample in the Groth strip. Fourteen of these overlap with sources in our Table 1. The remaining 9 do not, either because the source lies outside the region of the field we used or outside the redshift range we used, or because we found the $\text{Ly}\alpha$ identification to be dubious, or because we classified the source as an AGN based on the UV spectrum. Of the 14 sources in common, the classifications agree for 11 (3 AGNs and 8 star formers). We could not classify GALEX1420+5306, the first of the remaining 3 overlapped sources, as it has very weak emission lines. Finkelstein et al. (2009b) found this source, which they called EGS1, to be an AGN based on its $[\text{NII}]\lambda 6584/\text{H}\alpha$ ratio. As discussed in Cowie et al. (2010), we believe the second of the remaining 3 overlapped sources, GALEX1417+5224 (EGS2), is a high-excitation, very low metallicity galaxy rather than an AGN. Finally, we find that the third source, GALEX1421+5239 (EGS14), lies on the star-forming galaxy track in the BPT diagram. We do not detect high-ionization lines. This is in contrast to Finkelstein et al. (2009b), who classified the source as an AGN on the basis of both its position on the BPT diagram and the presence of high-ionization lines in its spectrum.

All eight of the $z = 0.65 - 1.25$ LAEs in Table 2 have been optically observed (Figures 1 and 2), and in all cases the $\text{Ly}\alpha$ identification is confirmed with the optical redshift. Seven of these have strong emission lines, and none of them shows $[\text{NeV}]$ emission or broad $\text{MgII}\lambda 2800$ emission that might classify the source as an AGN. The remaining source (GALEX1420+5313; see Figure 2(e)) has a post-starburst spectrum. (This galaxy is also identified in the DR3 release of the DEEP2 survey; Davis et al. 2007.) We label it as “A” in column 8 of Table 2 for its weak optical emission lines. It is possible that the $\text{Ly}\alpha$ emission is AGN-dominated in this galaxy. We therefore exclude this source from the $z = 0.65 - 1.25$ LAE sample.

Throughout our subsequent analysis we restrict to the LAEs that are confirmed as star formers from the optical spectra. We eliminate all sources with AGN signatures in either the optical or UV (including those sources identified as AGNs based on the BPT diagram), and we also eliminate the optically unobserved galaxies, the unconfirmed galaxies, and the galaxies with weak optical emission lines. This leaves a sample of 40 LAEs with rest-frame $\text{EW}(\text{Ly}\alpha) \geq 20 \text{ \AA}$ in the $z = 0.195 - 0.44$ interval and a sample of 5 LAEs with $\text{EW}(\text{Ly}\alpha) \geq 20 \text{ \AA}$ in the $z = 0.65 - 1.25$ interval.

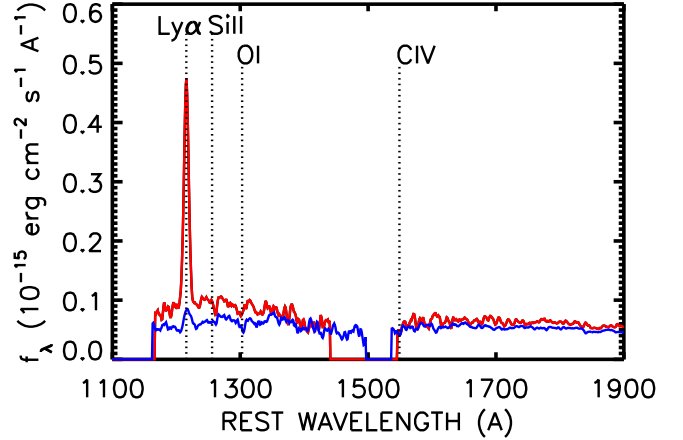


FIG. 5.— The average UV spectra of the 40 $z = 0.195 - 0.44$ LAEs (red spectrum) and of the 101 UV-continuum sources with rest-frame $\text{EW}(\text{H}\alpha) > 5 \text{ \AA}$ (blue spectrum). The gaps in the spectra correspond to the wavelength region between the FUV and NUV GALEX grisms. In addition to $\text{Ly}\alpha$, we mark the positions of UV absorption features that are only weakly seen in these low-resolution spectra.

In Figure 5 we compare the average UV spectrum of the 40 $z = 0.195 - 0.44$ LAEs (red spectrum) with that of the UV-continuum sample in the same redshift interval (blue spectrum). In order to make the most direct comparison, we eliminate weak emission-line galaxies with rest-frame $\text{EW}(\text{H}\alpha) < 5 \text{ \AA}$ in the UV-continuum sample, since we have eliminated these sources from the LAE sample. We also eliminate two objects which are classified as BPT AGN in the UV-continuum sample. This leaves 101 UV-continuum galaxies. However, including the remaining galaxies makes no difference to the results.

The NUV normalizations are almost identical since the samples are chosen with the same distribution of NUV magnitudes. The shapes are also nearly indistinguishable above 1400 \AA . By selection the LAE sample has strong emission, and the average spectrum for this sample has a rest-frame $\text{EW}(\text{Ly}\alpha) = 36 \text{ \AA}$. While a stacking procedure is not the best way to analyze objects with a mixture of $\text{Ly}\alpha$ emission and absorption, it at least allows us to see that the UV-continuum sample has $\text{Ly}\alpha$ emission and that its stacked spectrum is flatter than that of the LAE sample below 1400 \AA . Fitting the $\text{Ly}\alpha$ emission, we find a rest-frame $\text{EW}(\text{Ly}\alpha) = 7 \text{ \AA}$ for the emission feature. This is comparable to, but slightly higher than, the median value of $\text{EW}(\text{Ly}\alpha) = 4 \text{ \AA}$ found for the $z \sim 3$ LBG population by Kornei et al. (2010). The $z \sim 3$ LBG sample includes the LAEs as a subsample; thus, if anything, our sample, which excludes the LAEs, should be lower.

4. LAE LUMINOSITY EVOLUTION

A rest-frame $\text{EW}(\text{Ly}\alpha) \geq 20 \text{ \AA}$ is normally used to define the high-redshift LAE population (e.g., Hu et al. 1998), so in this section we apply that criterion. In Figure 6 we plot $\text{Ly}\alpha$ luminosity versus redshift and compare it with the measured luminosities of high-redshift LAE samples taken from Shimasaku et al. (2006), Ouchi et al. (2008), and Hu et al. (2010), all of which were chosen with the same EW selection criterion.

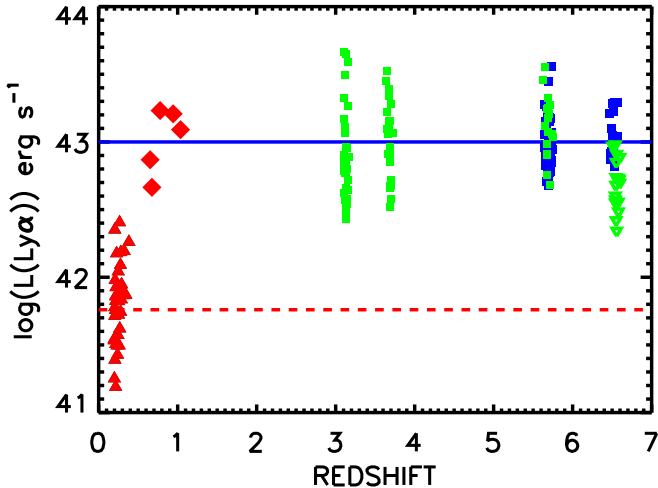


FIG. 6.— $\text{Ly}\alpha$ luminosity vs. redshift for the LAEs ($z = 0.195 - 0.44$ — small red triangles; $z = 0.65 - 1.25$ — larger red diamonds). Only sources with rest-frame $\text{EW}(\text{Ly}\alpha) \geq 20 \text{ \AA}$ are shown. At higher redshifts we show the $\text{Ly}\alpha$ luminosities from Ouchi et al. (2008) (green squares), Shimasaku et al. (2006) (green downward pointing triangles), and Hu et al. (2010) (blue squares). The red dashed line shows the L_* derived by Cowie et al. (2010) from a Schechter (1976) function fit to the $z = 0.195 - 0.44$ luminosity function with a slope of $\alpha = -1.36$. The blue solid line shows the L_* at $z = 5.7$ for $\alpha = -1.36$ (Hu et al. 2010).

The primary conclusion that we draw from Figure 6 is that there is a dramatic change in the properties of the LAEs between $z = 1$ and $z = 0$. There are no sources in the $z = 0.195 - 0.44$ sample with luminosities close to those of the brightest LAEs at high redshifts, but such sources are present by $z \sim 1$. This is not simply a volume effect: Cowie et al. (2010) determined the LAE luminosity function in the $z = 0.195 - 0.44$ redshift interval and showed that the L_* for a Schechter (1976) function fit with $\alpha = -1.36$ (red dashed line) is a factor of 8 fainter than that measured by Gronwall et al. (2007) at $z \sim 3$ and more than an order of magnitude fainter than that measured by Hu et al. (2010) at $z = 5.7$ (blue solid line).

We have computed the $z = 0.65 - 1.25$ $\text{Ly}\alpha$ luminosity function for the observed sample using the $1/V$ technique (Felten 1976) with the accessible volumes calculated from the areas versus NUV magnitudes in the sample. We show the luminosity function with the open black squares in Figure 7. As discussed extensively in Deharveng et al. (2008) and Cowie et al. (2010), this $\text{Ly}\alpha$ luminosity function corresponds to sources with $\text{NUV} < 22$ and must be corrected for LAEs at fainter continuum magnitudes. In the redshift interval $z = 0.195 - 0.44$ most sources with $\text{Ly}\alpha$ luminosities in the $10^{42} - 10^{43} \text{ erg s}^{-1}$ range lie at $\text{NUV} < 22$ and the corrections are small (Cowie et al. 2010). In contrast, many of the LAEs with $\text{Ly}\alpha$ luminosities $\sim 10^{43} \text{ erg s}^{-1}$ at $z = 0.65 - 1.25$ are fainter than $\text{NUV} > 22$ and the correction is substantial. Following the procedures outlined in Deharveng et al. (2008) and Cowie et al. (2010), we have computed the correction by assuming the $z \sim 1$ NUV counts derived from the luminosity functions of Arnouts et al. (2005) and the shape of the equivalent width distribution derived in Cowie et al. (2010) for the $z = 0.195 - 0.44$ sample. (This shape is almost identical to that seen at $z \sim 3$ by Shapley et al. 2003.) We show the corrected

points with the solid squares in Figure 7.

We compare with the $\text{Ly}\alpha$ luminosity functions at $z \sim 0.3$ (blue curve), $z \sim 3$ (red curve), $z \sim 5.7$ (green solid curve), and $z \sim 6.5$ (green dashed curve) using the Schechter (1976) function fits given in Cowie et al. (2010), Gronwall et al. (2007), and Hu et al. (2010). Even allowing for the small numbers in the present sample and the substantial corrections, we can see that there is a dramatic evolution in the luminosity function between $z \sim 0.3$ and $z \sim 0.95$. The data do not justify a Schechter (1976) function fit, but we show the Gronwall et al. (2007) luminosity function with L_* reduced by a factor of 2.5 as the black dashed curve. This function ($\phi_* = 1.28 \times 10^{-3}$, $\alpha = -1.36$, and $\log L_* = 42.26$) provides a reasonable fit to the data, though it is by no means unique. It would imply a reduction by a factor of 2.5 in the $\text{Ly}\alpha$ luminosity density between $z = 3$ and $z = 1$, which is much smaller than the dramatic factor of 50 reduction that Cowie et al. (2010) estimate between $z = 3$ and $z = 0.3$. This suggests that much of the evolution occurs in the $z = 0 - 1$ range, as is seen in many other populations.

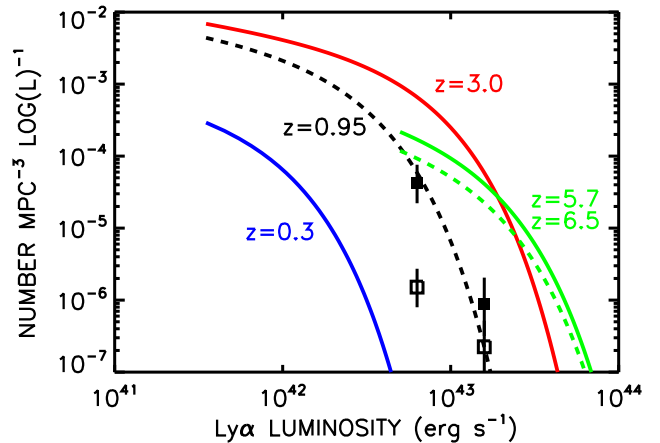


FIG. 7.— The derived $\text{Ly}\alpha$ luminosity function at $z = 0.65 - 1.25$ (black squares). The open squares show the values calculated for the present sample, which is drawn from galaxies with $\text{NUV} < 22$. The solid squares show the values corrected to allow for sources with fainter continuum magnitudes (see text). The error bars are $\pm 1\sigma$ from the Poisson errors corresponding to the number of sources in the bin. The blue curve shows the Schechter (1976) function fit to the $\text{Ly}\alpha$ luminosity function at $z = 0.194 - 0.44$ from Cowie et al. (2010), the red curve shows the fit at $z = 3$ from Gronwall et al. (2007), and the green curves show the fits at $z = 5.7$ (solid) and $z = 6.5$ (dashed) from Hu et al. (2010). The black dashed curve shows the Gronwall et al. luminosity function with L_* reduced by a factor of 2.5 to fit the $z = 0.65 - 1.25$ points.

5. WHAT ARE THE LAES?

5.1. Overview

We now turn to the $z = 0.195 - 0.44$ samples alone and what they can tell us about how LAE galaxies are drawn from the more general UV-continuum selected galaxy population. In this section we will occasionally include the LAEs with $\text{EW}(\text{Ly}\alpha) < 20 \text{ \AA}$ from the Table 1 supplement when this is appropriate. We parameterize the data with the rest-frame $\text{EW}(\text{H}\alpha)$. Using the $\text{EW}(\text{H}\alpha)$ allows us to intercompare easily the properties of the $\text{Ly}\alpha$ and UV-continuum samples. In addition, the $\text{EW}(\text{H}\alpha)$ is a rough measure of the age of a galaxy or, more precisely,

its specific SFR (SSFR), since the conversion from SSFR to age is dependent on the star formation history of the source (e.g., Leitherer et al. 1999). To zeroth order we may also expect the $\text{EW}(\text{H}\alpha)$ to be independent of extinction. In contrast, the complex escape path of the $\text{Ly}\alpha$ photons relative to the continuum photons combined with the effects of extinction may result in substantial changes in the $\text{EW}(\text{Ly}\alpha)$. These have been observed by some as decreases (Shapley et al. 2003; Pentericci et al. 2009) but not by others (Atek et al. 2008; Finkelstein et al. 2009c). We note, however, that even the $\text{EW}(\text{H}\alpha)$ may have some dependence on extinction, since the stars producing the ionizing photons may lie in different spatial regions of the galaxy than those producing the optical continuum photons.

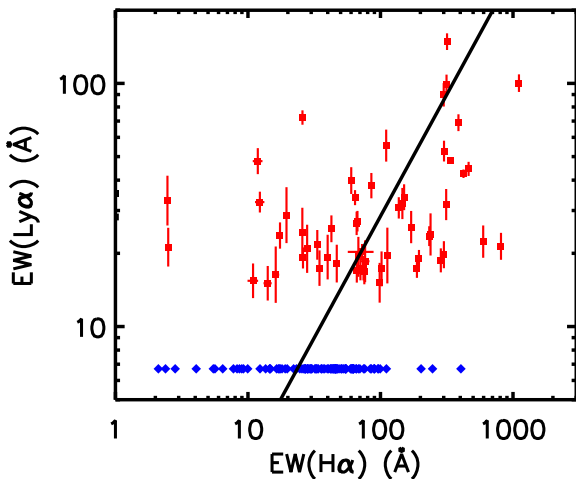


FIG. 8.— The rest-frame $\text{EW}(\text{Ly}\alpha)$ vs. the rest-frame $\text{EW}(\text{H}\alpha)$. The red squares show the LAE galaxies (the error bars are $\pm 1\sigma$), including those with rest-frame $\text{EW}(\text{Ly}\alpha)$ between 15 and 20 Å from the supplement to Table 1. The blue diamonds show the UV-continuum sample placed at the average $\text{EW}(\text{Ly}\alpha) = 7$ Å that was measured from the stacked spectrum. The positioning of these objects in y is purely for display purposes and is not used in the analysis. The black line shows a linear relation corresponding to the median $\text{EW}(\text{H}\alpha)/\text{EW}(\text{Ly}\alpha) = 3.5$ that was measured from the full LAE sample with rest frame $\text{EW}(\text{Ly}\alpha) > 15\text{Å}$.

While in the absence of dust we may expect the flux of $\text{Ly}\alpha$ to be related to that of $\text{H}\alpha$ by the case B ratio (8.7 for a temperature of 10,000 K; Brocklehurst 1971), the relation between the $\text{EW}(\text{H}\alpha)$ and the $\text{EW}(\text{Ly}\alpha)$ is more complex because of the relative evolution of the continuum fluxes. The $\text{EW}(\text{Ly}\alpha)$ declines rapidly after a single burst of star formation, as does the $\text{EW}(\text{H}\alpha)$. However, for a constant SFR model, the $\text{EW}(\text{Ly}\alpha)$ instead becomes roughly constant, since the UV-continuum flux and the $\text{Ly}\alpha$ line strength are governed by ongoing massive star formation (Charlot & Fall 1993; Schaerer & Verhamme 2008). In contrast, the $\text{EW}(\text{H}\alpha)$ continues to decline, even for a constant SFR model, as the older stars build up in the galaxy. For a galaxy with a large old population in place, the onset of a new burst of star formation will give a high $\text{EW}(\text{Ly}\alpha)$ while leaving the $\text{EW}(\text{H}\alpha)$ relatively weak. It is this ongoing build-up of the older stars that makes the $\text{EW}(\text{H}\alpha)$ a function of the age of the source.

In Figure 8 we show the rest-frame $\text{EW}(\text{Ly}\alpha)$ versus the rest-frame $\text{EW}(\text{H}\alpha)$ for the LAE galaxies (red squares), including those with rest-frame $\text{EW}(\text{Ly}\alpha)$ between 15 and

20 Å from the supplement to Table 1. We also show the spread of the $\text{EW}(\text{H}\alpha)$ for the UV-continuum sample (blue diamonds). While there is a large scatter, there is a broad general trend for the LAEs to have higher $\text{EW}(\text{H}\alpha)$. Specifically, we find that in the $\text{EW}(\text{Ly}\alpha) \geq 20$ Å and $\text{EW}(\text{Ly}\alpha) = 15 - 20$ Å samples, the median $\text{EW}(\text{H}\alpha)$ is 113 (66 – 233) Å and 71 (47 – 77) Å, respectively, while in the UV-continuum sample, it is 38 (31 – 44) Å, where the quantities in parentheses are the 68% confidence range. A Mann-Whitney rank-sum test gives less than a 3×10^{-6} probability that the distribution of $\text{EW}(\text{H}\alpha)$ is the same in the LAE sample as in the UV-continuum sample. For the 12 highest $\text{EW}(\text{Ly}\alpha)$ objects with rest-frame $\text{EW}(\text{Ly}\alpha) \geq 40$ Å the rank sum test give less than a 8×10^{-3} probability that the distribution of $\text{EW}(\text{H}\alpha)$ is the same as that for those with weaker EWs between 15 and 40 Å. This suggests that the LAEs are preferentially drawn from the younger galaxies in the sample.

These results differ from those of Östlin et al. (2009), who suggested, based on their observations of local blue compact galaxies, that there might be an anti-correlation between $\text{EW}(\text{Ly}\alpha)$ and $\text{EW}(\text{H}\alpha)$. As Östlin et al. noted, their small sample is highly selected and their result is not statistical. The Östlin et al. sample does emphasize, however, that there are galaxies such as SBS 0335-052 that have a very high $\text{EW}(\text{H}\alpha) = 1434$ Å but do not have strong $\text{Ly}\alpha$ emission. We do not detect any sources this extreme in our UV-continuum sample, where only four sources even have $\text{EW}(\text{H}\alpha) > 100$ Å, so they are clearly rare.

We can take this further by comparing other properties of the galaxies with the $\text{EW}(\text{H}\alpha)$. In Figure 9 we plot the following versus the rest-frame $\text{EW}(\text{H}\alpha)$: (a) the SDSS $u' - z'$ colors, (b) the FWHM of the galaxies in the CFHT U -band images, (c) the UV spectral index, (d) the flux ratio $f(\text{H}\beta)/f(\text{H}\alpha)$, (e) the flux ratio $f(\text{Ly}\alpha)/f(\text{H}\alpha)$, and (f) the logarithm of the flux ratio $f([\text{NII}]\lambda 6584)/f(\text{H}\alpha)$. Panel (b) is restricted to the subsample covered by the U -band CFHT images, while panels (a), (d), and (e) correspond to the subsample covered by the SDSS observations. Panels (c) and (f) contain the full sample. In panel (a) we have used the spectra to correct for the contributions of emission lines to the z' magnitude (see Section 5.2), since these can make significant contributions that are a function of the $\text{EW}(\text{H}\alpha)$. We now consider each of these relations in detail.

5.2. Colors and Ages

The $u' - z'$ colors of Figure 9(a) follow a single well-defined track (see also Overzier et al. 2008, who show a similar figure for their low-redshift analogs to the LBGs). We compare the data with a constant star formation model (solid curve) computed with the STARBURST99 code (Leitherer et al. 1999). Here the $\text{EW}(\text{H}\alpha)$ decreases as the age increases so time increases to the left in the plot. The predicted evolution of the $u' - z'$ color versus the $\text{EW}(\text{H}\alpha)$ up to an age of 10^9 yr matches to the emission-line corrected colors. By contrast, a single starburst (dashed curve) does not match, since the $\text{EW}(\text{H}\alpha)$ drops rapidly with time, while the $u' - z'$ colors remain blue.

We can use the full color information to infer ages and extinctions by spectral energy distribution (SED) fitting. For sources with strong optical emission lines we empha-

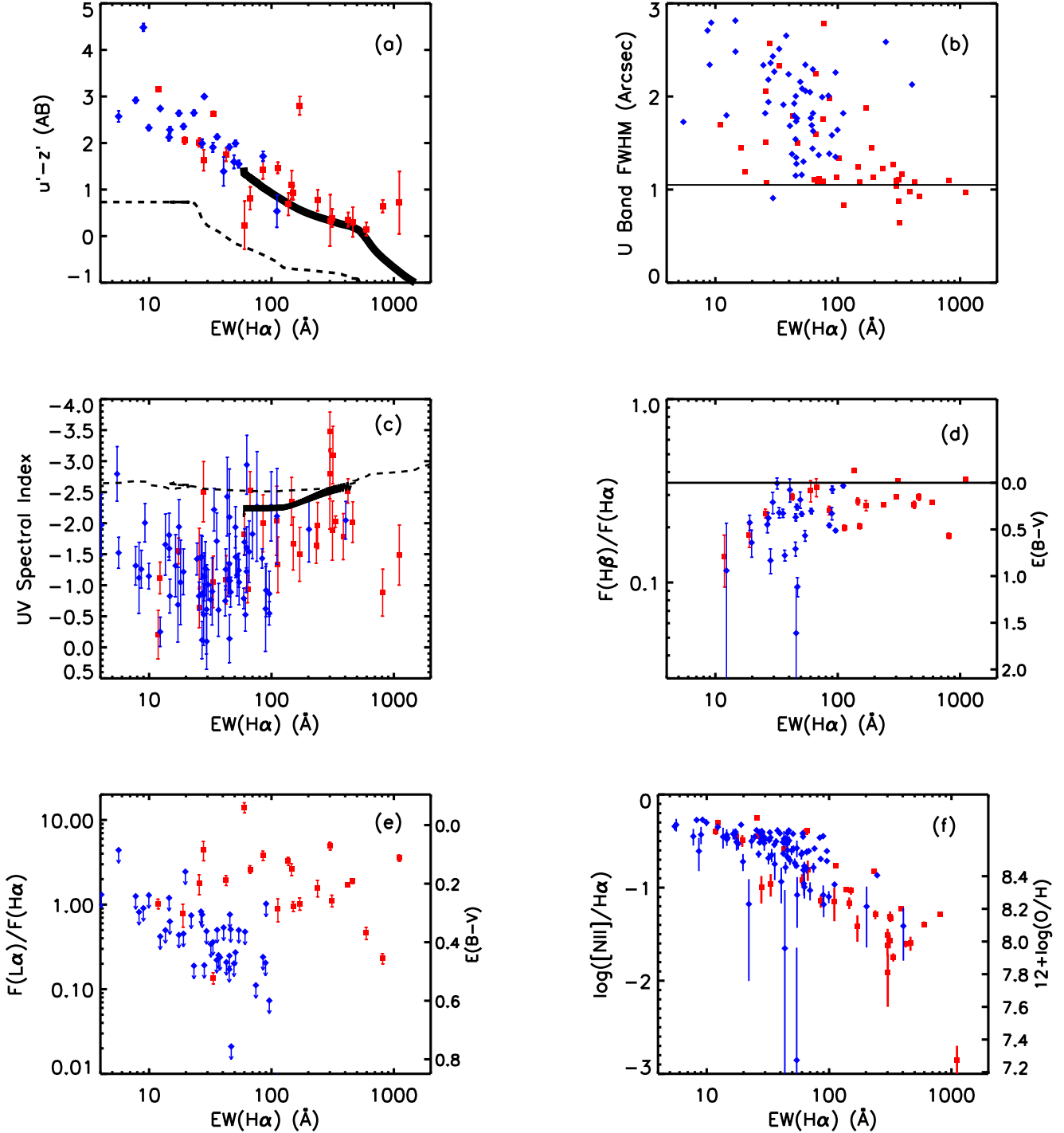


FIG. 9.— The (a) SDSS $u' - z'$ color, (b) FWHM in CFHT MegaPrime U -band images, (c) UV power law slope, (d) $f(H\beta)/f(H\alpha)$, (e) $f(L\alpha)/f(H\alpha)$, and (f) $\log(f([NII]\lambda 6584)/f(H\alpha))$, all plotted vs. the rest-frame $EW(H\alpha)$. The red squares show the LAE galaxies with $EW(L\alpha) \geq 20 \text{ \AA}$. The blue diamonds show the UV-continuum sample. Error bars are $\pm 1\sigma$. In (a) we have used the spectra to correct for the emission-line contributions to the z' magnitude (see Section 5.2). In (a) and (c) the black curves show solar metallicity models from STARBURST99 with no extinction: a constant SFR model (thick solid) and a single instantaneous starburst model (dashed). The right-hand axes in (d) and (e) show the $E(B-V)$ values that would be derived from the Calzetti et al. (2000) reddening law. The right-hand axis in (f) shows the O abundance that would be derived from $f([NII]\lambda 6584)/f(H\alpha)$ using the Pettini & Pagel (2004) conversion.

size that it is critical to remove the substantial line contributions. The correction is a function of the $\text{EW}(\text{H}\alpha)$ and hence introduces a systematic bias into any comparison of LAEs with UV-continuum selected galaxies. For strong-line sources SED fitting to the uncorrected data substantially overestimates the ages. This then causes the extinctions to be underestimated and the masses to be overestimated.

We illustrate the problem in Figure 10, where we show the broadband fluxes before (black open squares) and after (red diamonds) line correction for three LAE galaxies spanning a wide range in the $\text{EW}(\text{H}\alpha)$. The strong $[\text{OIII}]\lambda 5007$ and $\text{H}\alpha$ line contributions raise the SED at wavelengths above 4000 Å. In the fitting procedure this is spuriously interpreted as a strong 4000 Å break, which results in a substantial age overestimate. The strongest emitters (Figures 10(a) and 10(b)) are, in fact, very young but are misinterpreted as having ages of 0.45 and 0.9 Gyr when fits to the uncorrected data are used.

We have fitted ages and extinctions for all of the galaxies covered by the SDSS in both the LAE and UV-continuum samples. We used the Bruzual & Charlot (2003) models with solar metallicities and a range of exponentially declining SFR models with e-folding times from 1 Gyr to 20 Gyr. We combined these with a Calzetti et al. (2000) extinction law. For each star formation history we determined the age and extinction that produced a χ^2 minimized fit using the measured errors in the broadband fluxes, together with a 10% error to allow for systematic uncertainties.

It is well known that the $\text{EW}(\text{H}\alpha)$ can be used as an age indicator (e.g., Leitherer et al. 1999; Bruzual & Charlot 2003). We plot the galaxy ages determined from the SED fits versus the $\text{EW}(\text{H}\alpha)$ in Figure 11. In Figure 11(a) we show the spurious ages that would be derived from a simple fit to the data without the emission-line corrections. In Figure 11(b) we show the ages derived from the corrected broadband fluxes. The inferred ages are somewhat degenerate with the assumed exponential star formation history, so we also show the range of ages corresponding to the range of SFR models to give a measure of the modeling uncertainties. We can see from Figure 11(a) that nearly all of the sources with strong $\text{EW}(\text{H}\alpha)$ are assigned ages of about a Gyr. Thus, without the line correction, we would consider there to be no difference in age for a wide range of $\text{EW}(\text{H}\alpha)$. However, we can see from Figure 11(b) that when the line correction is made, we obtain a smooth evolution in age with the strongest $\text{EW}(\text{H}\alpha)$ sources having the lowest ages of about 10 Myr. The high $\text{EW}(\text{H}\alpha)$ sources are quite well described by a constant SFR model (black solid curve in Figure 11(b)), but at lower $\text{EW}(\text{H}\alpha)$, the sources tend to fall below this curve, presumably as the SFR begins to decline. The data are quite well represented by a single power law fit

$$\log T = 5.48 \pm 0.23 + (-1.53 \pm 0.12) \times \log(\text{EW}(\text{H}\alpha)), \quad (1)$$

where the age T is in Myr and the $\text{EW}(\text{H}\alpha)$ is in Å. This is shown by the green dashed line in Figure 11(b).

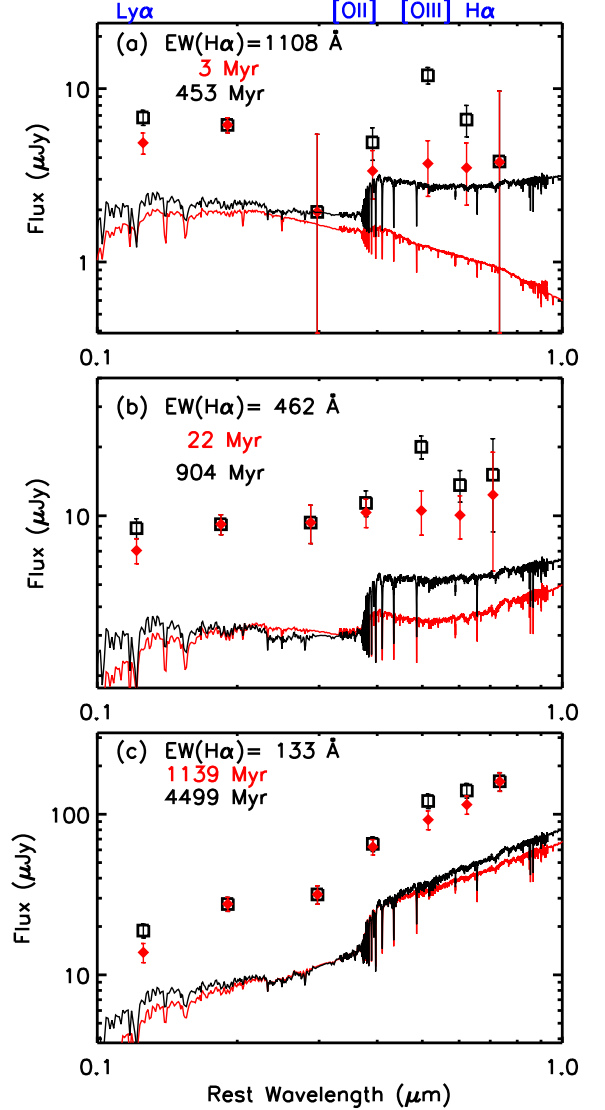


FIG. 10.— SEDs before (black open squares) and after (red solid diamonds) removal of the emission-line contributions. Each panel shows a LAE galaxy with the rest-frame $\text{EW}(\text{H}\alpha)$ given in the upper-left corner. For each spectrum we removed the $\text{Ly}\alpha$, $[\text{OII}]\lambda 3727$, $\text{H}\gamma$, $\text{H}\beta$, $[\text{OIII}]\lambda 4959$ and $\lambda 5007$, $\text{H}\alpha$, $[\text{NII}]\lambda 6548$ and $\lambda 6584$, and $[\text{SII}]\lambda 6716$ and $\lambda 6738$ emission lines using the Gaussian fits. We then integrated the spectrum (with and without the lines) through the filter response to determine the fraction of the light that is produced by the continuum and used this to correct the magnitudes. The principal contributing lines are marked at the top of the figure. The error bars are $\pm 1\sigma$, including a 10% flux error to allow for possible systematic errors in the determination of the total magnitudes. The line effects are the largest for the higher $\text{EW}(\text{H}\alpha)$ galaxies. The corrections act to smooth the SEDs. For each galaxy we show the constant SFR model fits from Bruzual & Charlot (2003). The black (red) curve shows the fit to the raw (corrected) data. Both are reduced by a factor of three so the data points can be clearly seen. The fitted ages are shown in the upper left corner for the raw fit (black) and for the line-corrected fit (red).

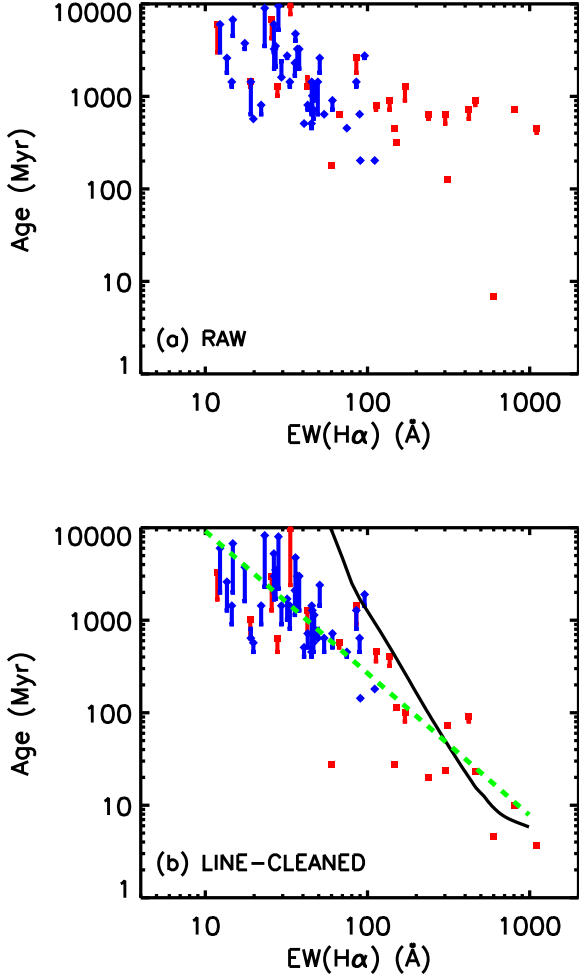


FIG. 11.— The ages determined from spectral synthesis fitting to the Bruzual & Charlot (2003) models vs. the $EW(H\alpha)$. In (a) we show the ages derived when no correction is applied for the emission lines. In (b) we show the ages derived when the broadband colors are properly corrected. For each object (red squares—LAE galaxies with $EW(Ly\alpha) \geq 20$ Å; blue diamonds—UV-continuum sample) we show the range of ages corresponding to the models with exponentially declining SFRs with e-folding times from 1 Gyr to 20 Gyr (vertical bars). The data point corresponds to the 20 Gyr case. In (b) the black solid curve shows the age vs. the $EW(H\alpha)$ relation for a constant SFR model computed with STARBURST99, and the green dashed line shows the optimal power law fit given in the text.

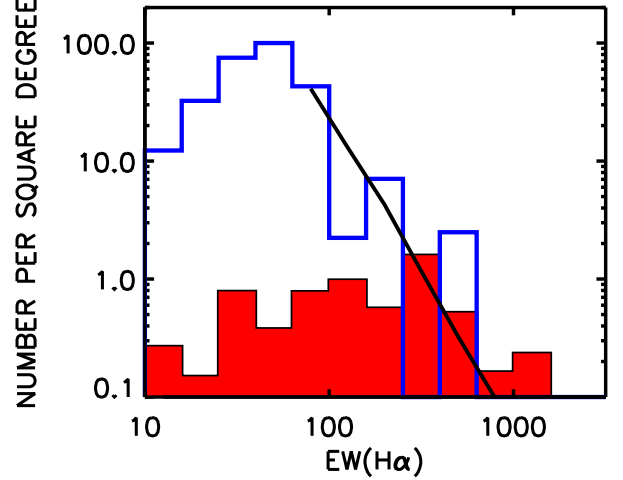


FIG. 12.— The surface density of sources vs. the $EW(H\alpha)$. The red shaded histogram shows the LAE galaxies with rest-frame $EW(Ly\alpha) \geq 20$ Å. The blue histogram shows the UV-continuum sample, which is much more heavily weighted to low values of the $EW(H\alpha)$. The black solid curve shows the shape computed from a model where we assume a constant rate of formation of galaxies and that the time spent in each equivalent width bin is determined from Equation 1. The normalization is matched to the observed surface density.

In Figure 12 we plot the surface densities of galaxies in our LAE and UV-continuum samples versus the $EW(H\alpha)$. It is worth emphasizing that in both the LAE and UV-continuum samples the galaxies are chosen solely on the basis of their NUV magnitudes; that is, they have $NUV < 22.1$, lie in the redshift interval $z = 0.195 - 0.44$, and have the same NUV magnitude distribution. The only difference between the two samples is the presence or absence of strong $Ly\alpha$ emission. Thus, while there might be a relation between the NUV magnitude and the $EW(H\alpha)$, this will operate in the same way in both samples and will not affect any comparison.

For the LAE sample (red shaded histogram) we plot the sum of the inverse areas over which a galaxy with a given NUV magnitude could be observed in the *GALEX* fields (Cowie et al. 2010). (We also corrected the LAE density for the 10% of sources that were not spectroscopically observed.) For the UV-continuum sample (blue histogram) we also weight the areas with the fraction of sources that we observed as a function of NUV magnitude. The black solid curve shows the shape computed from a model where we assume a constant rate of formation of galaxies and that the time spent in each equivalent width bin is determined from Equation 1. The normalization is proportional to the birthrate of galaxies, and we have matched it to the observed surface density. We can see that this model matches well to the shape at high $EW(H\alpha)$, so the surface density of galaxies versus the $EW(H\alpha)$ is also consistent with a constant production rate of new galaxies that then evolve with a constant SFR.

We can also see from the figure that $Ly\alpha$ emission is rare in sources with $EW(H\alpha) < 100$ Å (about 0.7% of galaxies) but common in higher $EW(H\alpha)$ sources where the blue and red histograms become comparable. $31 \pm 13\%$ of the $EW(H\alpha) > 100$ Å galaxies and $57 \pm 30\%$ of the $EW(H\alpha) > 250$ Å galaxies have $Ly\alpha$ emission with the

$\text{EW}(\text{Ly}\alpha) \geq 20 \text{ \AA}$. The uncertainties reflect the small number of UV-continuum sources with high $\text{EW}(\text{H}\alpha)$. Finally, we can see that a large fraction of the LAEs ($75 \pm 12\%$) are drawn from the high $\text{EW}(\text{H}\alpha) > 100 \text{ \AA}$ population. This again shows that the LAEs are drawn primarily from the youngest galaxies. The remaining 25% of LAEs with $\text{EW}(\text{H}\alpha) < 100 \text{ \AA}$ may have geometries, kinematics, or orientations that are unusually conducive to $\text{Ly}\alpha$ escape. However, some may be objects where the $\text{Ly}\alpha$ emission is produced by AGN activity, but the AGN signatures in the optical are swamped by the galaxy contributions.

In the following sections we will use the $\text{EW}(\text{H}\alpha) = 100 \text{ \AA}$ as a rough cut above which $\text{Ly}\alpha$ emission is more common.

5.3. Sizes

Figure 9(b) shows that there is also a size evolution as a function of $\text{EW}(\text{H}\alpha)$. The higher $\text{EW}(\text{H}\alpha)$ sources are generally unresolved at the $\sim 1''$ resolution of the CFHT MegaPrime U -band images, while the lower $\text{EW}(\text{H}\alpha)$ sources are generally extended. However, unlike in the other correlations, there is a significant difference between the LAEs and the UV-continuum sources at the same $\text{EW}(\text{H}\alpha)$. From Figure 9(b) we can see that at the same $\text{EW}(\text{H}\alpha)$, sources with $\text{Ly}\alpha$ emission are significantly smaller than those without; that is, where $\text{Ly}\alpha$ is strong is in the most compact sources at a given $\text{EW}(\text{H}\alpha)$. A rank-sum test shows that there is a $< 3.6 \times 10^{-5}$ probability that the LAEs at $\text{EW}(\text{H}\alpha) > 80 \text{ \AA}$ are physically as large as the UV-continuum sources with the same $\text{EW}(\text{H}\alpha)$ selection. (We have chosen the $\text{EW}(\text{H}\alpha)$ to provide a significant number of UV-continuum sources since there are only 4 UV-continuum sources with $\text{EW}(\text{H}\alpha) > 100 \text{ \AA}$ as can be seen in Figure 9(b)). The median FWHM for these LAEs is $1.1''$, comparable to the resolution in the CFHT MegaPrime images, while that for the UV-continuum sources with the same $\text{EW}(\text{H}\alpha)$ selection is $1.6''$.

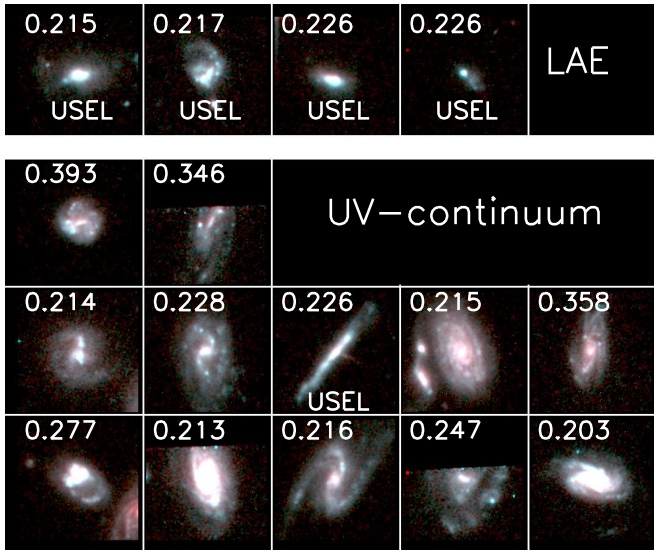


FIG. 13.— Images from the GEMS survey of the CDF-S. The lower 12 sources are UV-continuum sources in the region, and the top 4 sources are LAEs. Each thumbnail is $6''$ on a side. The blue and green colors correspond to the F606W GEMS image, and the red color corresponds to the F850W GEMS image.

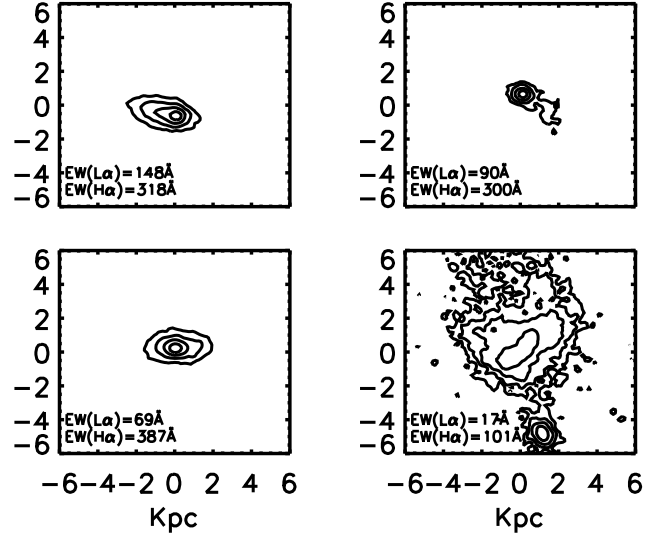


FIG. 14.— Contour plots for the 4 LAEs in the GEMS survey of the CDF-S. Each contour in the combined F606W and F850W image rises by a factor of two. The rest-frame $\text{EW}(\text{Ly}\alpha)$ and the rest-frame $\text{EW}(\text{H}\alpha)$ are given in the lower-left corner.

The ground-based U -band imaging is inadequate to resolve the sizes for most of the LAEs. Thus, although the optical morphologies may differ from those in the UV, here we use *HST*-based images to obtain rest-frame optical sizes. In Figure 13 we show the combined F606W and F850W *HST* ACS images for the sources that lie in the GEMS survey field. In Figure 14 we show the contours from the combined F606W and F850W images for the four LAEs. The FWHM in these higher resolution images is 0.5 kpc for the three sources with $\text{EW}(\text{Ly}\alpha) \geq 20 \text{ \AA}$, though the one source with $\text{EW}(\text{Ly}\alpha) < 20 \text{ \AA}$ is more extended with a FWHM of about 2 kpc . These sizes are very similar to the continuum sizes of LAEs in the rest-frame UV at $3 < z < 6.5$ (Bond et al. 2009, 2010; Cowie et al. 2011) though again we emphasize that it would be desirable to make the comparison at the same rest-frame wavelength.

5.4. Extinction

We can measure the dust extinction from the galaxies in several ways: from the UV spectral slopes, from the SED fits, and from the Balmer ratios. We may intercompare these measurements and also use each of them to test the effects of extinction on the $\text{Ly}\alpha$ line.

In Figure 9(c) the UV spectral index, which is often used as a measure of the stellar extinction, shows a general trend towards less negative values as we move to lower $\text{EW}(\text{H}\alpha)$, which would be expected if the extinction is rising as the galaxies age. However, there is a good deal of scatter, and at least part of the change is caused by evolution in the intrinsic spectrum. The evolution of the reddening may be more clearly seen in Figure 9(d): the Balmer ratio shows a systematic decrease as the $\text{EW}(\text{H}\alpha)$ decreases, indicating an increase in the nebular extinction. The derived $E(B-V)$ is similar whether we use the Cardelli et al. (1989) extinction law or the Calzetti et al. (2000) extinction law. With the Calzetti et al. reddening we obtain a median $E(B-V)$ of 0.23 ($0.15, 0.32$) from the Balmer ratio for sources with $\text{EW}(\text{H}\alpha) > 100 \text{ \AA}$ and 0.33 ($0.30, 0.38$) for sources with $\text{EW}(\text{H}\alpha) = 20 - 100 \text{ \AA}$, where the

quantities in parentheses are the $\pm 1\sigma$ range. Interestingly, in both Figures 9(c) [UV spectral index versus $\text{EW}(\text{H}\alpha)$] and 9(d) [Balmer ratio versus $\text{EW}(\text{H}\alpha)$] there appears to be little differentiation between LAEs and UV-continuum galaxies at the same $\text{EW}(\text{H}\alpha)$, suggesting that extinction is not the primary reason for $\text{Ly}\alpha$ being suppressed at a given $\text{EW}(\text{H}\alpha)$. This is a well-known result which has been found by many authors (e.g., Giavalisco et al. 1996; Mas-Hesse et al. 2003; Atek et al. 2009b; Finkelstein et al. 2009a).

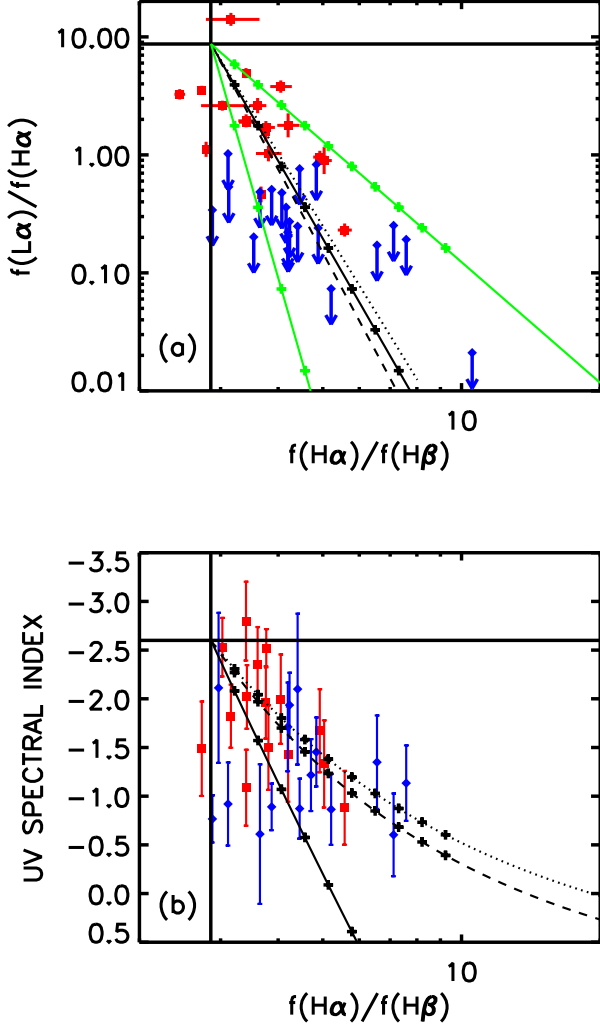


FIG. 15.— The evolution of (a) $f(\text{Ly}\alpha)/f(\text{H}\alpha)$ and (b) the UV spectral index vs. the Balmer ratio $f(\text{H}\alpha)/f(\text{H}\beta)$. All sources with rest-frame $\text{EW}(\text{H}\alpha) > 20 \text{ \AA}$ are shown (red squares — LAEs; blue diamonds — UV-continuum sources). The $\text{EW}(\text{H}\alpha)$ limit is chosen to include nearly all of the LAEs (see Figure 12) and to provide a sample of UV-continuum objects with strong $\text{H}\alpha$. The two figures contain slightly different sets of objects since the UV spectral indices are only measured for a limited redshift range. The upper limits on the $\text{Ly}\alpha$ fluxes for the UV-continuum galaxies are computed for an observed-frame $\text{EW}(\text{Ly}\alpha) = 10 \text{ \AA}$. The expected ratios are shown for several reddening laws: Calzetti et al. (2000; solid), Cardelli et al. (1989; dashed), and Fitzpatrick et al. (1999; dotted). The crosses on the curves show increments of 0.1 in $E(B-V)$ from the adopted intrinsic values, which are shown by the solid vertical and horizontal lines. In (a) the lower (upper) green line shows the expected relationship for the Calzetti et al. reddening law if the $E(B-V)$ is twice (half) as large for $\text{Ly}\alpha$ as for the Balmer lines.

As has been pointed out by Atek et al. (2009a) and Scarlata et al. (2009) based on the GALEX LAE samples (see also Hayes et al. (2010) for a discussion of a higher redshift sample), there is a relation between $f(\text{Ly}\alpha)/f(\text{H}\alpha)$ and $f(\text{H}\alpha)/f(\text{H}\beta)$ for LAE galaxies but with a wide dispersion. In Figure 15(a) we show such a plot for our LAE galaxies (red squares) and UV-continuum galaxies (blue diamonds) with $\text{EW}(\text{H}\alpha) > 20 \text{ \AA}$, where the $\text{H}\alpha$ limit is chosen to include nearly all the LAEs (see Figure 12). The upper limits on the $\text{Ly}\alpha$ fluxes for the UV-continuum galaxies are computed for an observed-frame $\text{EW}(\text{Ly}\alpha) = 10 \text{ \AA}$. We emphasize again that, unlike Atek et al. (2009a), our $\text{H}\alpha$ measurements are not matched to the GALEX aperture, so our $f(\text{Ly}\alpha)/f(\text{H}\alpha)$ ratio may have additional systematic scatter. In addition, the relative flux calibration and uncertainties in the underlying absorption correction for the $\text{H}\beta$ line may result in scatter in $f(\text{H}\alpha)/f(\text{H}\beta)$ and occasional unphysical values (negative extinction) in this ratio.

The inclusion of the UV-continuum sample shows that the LAEs correspond to the maximum values of $f(\text{Ly}\alpha)/f(\text{H}\alpha)$ at a given $f(\text{H}\alpha)/f(\text{H}\beta)$, as would be expected from the initial selection in the $\text{Ly}\alpha$ line. At any given $f(\text{H}\alpha)/f(\text{H}\beta)$ there is a range in $f(\text{Ly}\alpha)/f(\text{H}\alpha)$ stretching up to roughly the value set by simple extinction of the $\text{Ly}\alpha$ line if it followed the same escape path as the $\text{H}\alpha$ line. The LAEs primarily lie along this relation. The line followed by the LAEs is consistent either with the Calzetti et al. (2000) reddening law (black solid line) or with uniform screen models, such as those of Cardelli et al. (1989; black dashed) or Fitzpatrick et al. (1999; black dotted), all of which give nearly identical predictions. There is considerable scatter about the relation, but we suspect that this is a consequence of systematic errors in the flux calibration discussed above, rather than an indication of the need for more complex dust models, as suggested by Scarlata et al. (2009). We can also see that the data are not consistent with the $\text{Ly}\alpha$ photons in the LAE galaxies having a widely different $E(B-V)$ path from the $\text{H}\alpha$ photons. Following Scarlata et al., we have plotted the relation when the $\text{Ly}\alpha$ path is twice that of the Balmer photons (lower green line) and also when it is half that of the Balmer photons (upper green line). It is clear that these are a much poorer fit to the LAE observations.

In contrast, if we plot the UV spectral index for the same sample versus $f(\text{H}\beta)/f(\text{H}\alpha)$ (Figure 15(b)), then we see that the Calzetti et al. (2000) reddening law gives a substantially different result than the Cardelli et al. (1989) or Fitzpatrick et al. (1999) uniform screen models, reflecting their different shapes at UV wavelengths. Most of the data appear to follow the models of Cardelli et al. or Fitzpatrick et al. rather than the reddening law of Calzetti et al., though there are a handful of outlying points. This suggests that for these galaxies the stellar extinction is better represented as a uniform screen rather than a patchy distribution. This is the case for both the LAEs and the UV-continuum sources.

5.5. Metallicity

Perhaps the most interesting plot in Figure 9 is that of $\text{N2} = \log(f([\text{NII}]\lambda 6584)/f(\text{H}\alpha))$ versus $\text{EW}(\text{H}\alpha)$ (panel f). N2 is a widely used metallicity indicator with low values corresponding to low metallicities. The fact that both

the LAE and UV-continuum galaxies follow a surprisingly tight track in this diagram with N2 rising as $\text{EW}(\text{H}\alpha)$ decreases appears to show that we are seeing a smooth metal build-up with age in both classes of galaxies.

In order to translate N2 to a metallicity in the galaxies we use the Pettini & Pagel (2004) local relationship, $12 + \log(\text{O}/\text{H}) = 8.90 + 0.57\text{N}2$, which was determined by comparing to direct measures of the O abundance over the range $\text{N}2 = -2.5$ to -0.5 . Extrapolating the Pettini & Pagel relation to these galaxies requires assuming that there is no change in the ionization parameter, which may well be incorrect. However, at $z = 0.195 - 0.44$ Cowie & Barger (2008) found a narrow range of ionization parameters ($q \sim 2 \times 10^7$) and a similar relation to that of Pettini & Pagel. Cowie & Barger (2008) also showed that other line diagnostics gave similar metal-luminosity relations to that derived from N2 in the redshift interval $z = 0.195 - 0.44$.

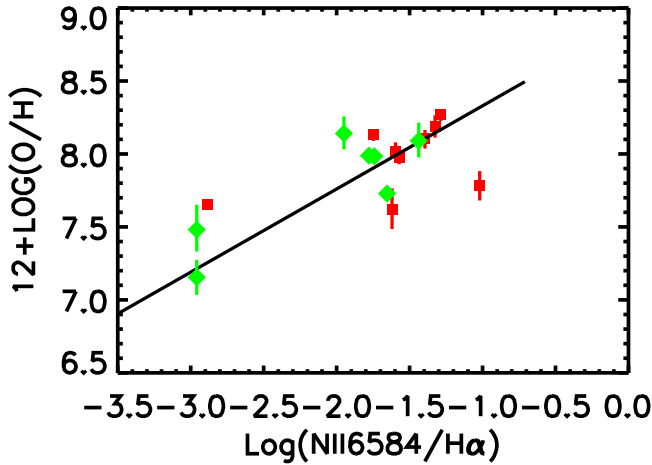


FIG. 16.— $12 + \log(\text{O}/\text{H})$ derived from the direct method vs. N2. The *GALEX* sources in the redshift interval $z = 0.195 - 0.44$ are shown with red squares with 1σ error bars. A sample of ultra-strong emission-line galaxies in the same redshift interval with direct O measurements from Hu et al. (2010) are shown with green diamonds. Both are broadly consistent with the Pettini & Pagel (2004) relation (black line), though with substantial scatter.

We can also test the Pettini & Pagel (2004) relation with the present data. Ten of the $z = 0.195 - 0.44$ sources have $[\text{OIII}]\lambda 4363$ detected at above the 3σ level. These are marked with green diamonds in Figure 4(a). None of the UV-continuum sample at $z = 0.195 - 0.44$ has detected $[\text{OIII}]\lambda 4363$ at the 3σ level. All of the $[\text{OIII}]\lambda 4363$ galaxies have low values of N2, except for *GALEX* 1240+6233, which is classified as an AGN based on the BPT diagram. Conversely, most of the low-N2 galaxies are detected in $[\text{OIII}]\lambda 4363$. For the sources that are not AGNs and where we have detected $[\text{OIII}]\lambda 4363$ we used the ‘direct’ or T_e method to determine the metallicity (e.g., Seaton 1975; Pagel et al. 1992; Pilyugin & Thuan 2005; Izotov et al. 2006). To derive $T_e[\text{OIII}]$ and the oxygen abundances, we used the Izotov et al. (2006) formulae, which were developed with the latest atomic data and photoionization models. We compare the derived O abundances with N2 in Figure 16 (red squares), where we also show similar measurements from a sample of ultra-strong emission-line galaxies taken from Hu et al. (2009; green diamonds). The O abundance versus N2 is broadly consistent with the Pet-

tini & Pagel relation (black line), though there is a good deal of scatter, probably reflecting the variation in the ionization parameter.

We can see immediately from Figure 9(f) that the LAEs in the redshift interval $z = 0.195 - 0.44$ have lower values of N2 than the UV-continuum sources (see also Figure 4). This effect was previously noted by Cowie et al. (2010), though the present larger sample substantially increases the statistical significance of the result. This result may be more clearly seen in Figure 17, where we show the N2 distributions for the LAE (red shaded histogram) and UV-continuum (blue histogram) samples. While the N2 distributions overlap, the distribution for the LAEs clearly extends to lower values, and the median N2 is lower. A rank-sum test gives only a 10^{-6} probability that the two *GALEX* samples are similar. Using the Pettini & Pagel (2004) conversion gives a median $12 + \log(\text{O}/\text{H}) = 8.24$ (8.17, 8.35) for the LAEs, where the quantities in parentheses are the $\pm 1\sigma$ range. This is about 0.4 dex lower than that of the UV-continuum sample, though the median value for the UV-continuum sample is more poorly determined, since at the higher values of N2 the conversion breaks down as the N2 value saturates.

We can now see from Figure 9(f) that the difference in N2 distributions is primarily a reflection of the evolutionary state of the galaxy. That is, the metallicity is building up with age, and the LAEs are preferentially drawn from the younger galaxies. UV-continuum galaxies have similar metallicities to LAEs with the same $\text{EW}(\text{H}\alpha)$. However, the LAE sample is much more weighted to high $\text{EW}(\text{H}\alpha)$ galaxies, which are younger and more metal poor.

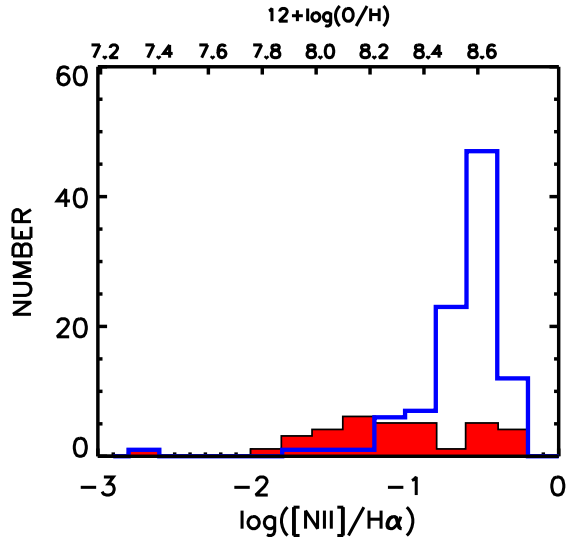


FIG. 17.— The number distributions of the LAE galaxies with $\text{EW}(\text{Ly}\alpha) \geq 20 \text{ \AA}$ (red shaded histogram) and the UV-continuum sample (blue histogram) as a function of N2. The UV-continuum sample is much more heavily weighted to high values of N2. The top axis shows the O abundance that would be derived from the N2 ratio using the Pettini & Pagel (2004) conversion.

6. THE PHYSICAL PROPERTIES OF THE GALAXY SAMPLES

In order to convert the observed quantities into physical properties of the galaxies, we will assume a constant SFR model with a Salpeter (1955) initial mass function (IMF). As we have seen, this appears to provide a self-consistent

fit to most of the observed properties. For simplicity, we assume that the IMF extends smoothly from $0.1 M_{\odot}$ to $100 M_{\odot}$, though this can be easily converted into other favored IMFs with flatter slopes below $M_{\odot} = 1$ by a simple renormalization of the SFR.

In Figure 18 we show the $H\alpha$ luminosities of the LAE and UV-continuum samples corrected for extinction using the Balmer ratio and a Fitzpatrick et al. (1999) extinction law. The median corrections for the LAE and UV-continuum samples are 1.7 and 2.1, respectively.

For our assumed constant SFR model the conversion from $H\alpha$ luminosity to SFR is roughly invariant over the range of $EW(H\alpha)$ and is given by the Kennicutt (1998) relation:

$$\log \text{SFR} = -41.1 + \log L(H\alpha). \quad (2)$$

On the right-hand axis of Figure 18 we give the SFR in $M_{\odot} \text{ yr}^{-1}$ corresponding to a given $H\alpha$ luminosity. Individual galaxies have SFRs that range from about $1 M_{\odot} \text{ yr}^{-1}$ up to about $30 M_{\odot} \text{ yr}^{-1}$. The lower bound is roughly set by the NUV magnitude limit for the selection, but the upper bound on the SFR is a measure of the maximum SFRs seen in UV-continuum selected galaxies at these redshifts. On the top axis we give the logarithm of the age in years corresponding to a given $EW(H\alpha)$. The LAEs are primarily drawn from sources younger than 1 – 2 Gyr.

We can see from Figure 18 that there is no evolution in the distribution of the SFRs as a function of the $EW(H\alpha)$. This is consistent with our constant SFR assumption. There is also no difference in the distribution of the SFRs for the LAE and UV-continuum galaxies. If the highest SFR galaxies maintain their rates for a substantial fraction of the local age of the universe, then the final stages will have stellar masses in excess of $10^{11} M_{\odot}$.

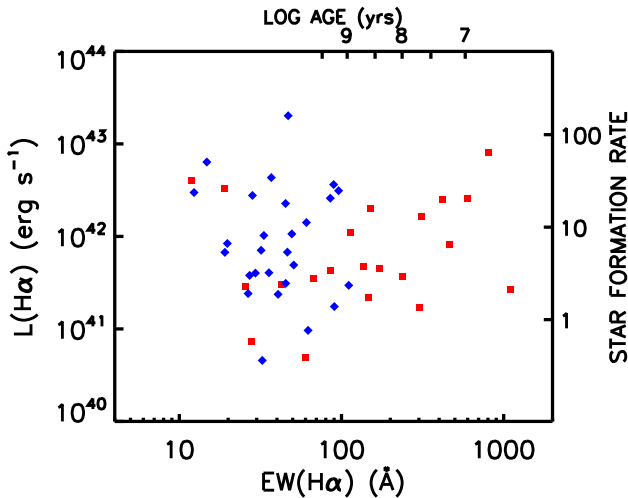


FIG. 18.— Extinction-corrected $H\alpha$ luminosity vs. $EW(H\alpha)$. The red squares show LAEs with $EW(Ly\alpha) \geq 20 \text{ \AA}$, and the blue diamonds show UV-continuum galaxies. The conversion to a SFR assuming a Salpeter (1955) IMF and a constant SFR is shown on the right-hand axis, and the conversion to galaxy age is shown on the top axis.

We can test our $H\alpha$ luminosity-determined SFRs against those inferred from 20 cm observations (where available; see Section 2.1) and those determined from the UV continuum. In Figure 19 we plot rest-frame 20 cm power calculated assuming a radio spectrum of $f_{\nu} \sim \nu^{-0.8}$ versus

extinction-corrected $H\alpha$ luminosity. We see a nearly linear relation, though the number of measured sources is fairly small. We compare the data with two conversions of the radio power to SFR: Condon (1992; solid line) and Bell (2003; dashed line). The two relations appear to bracket the data points. (Prior to the $H\alpha$ extinction correction the points are more scattered and fall to the left of the expected relations.)

There is one significantly deviant point, GALEX0959+0151 in COSMOS 00, where the $H\alpha$ luminosity is very high compared to the radio power. This source has the highest $EW(H\alpha)$ in the figure (811 \AA) and an age of 9 Myr from SED fitting (Figure 11(b)). This suggests that the radio power is low because the supernovae that generate the radio emission have yet to occur. Unfortunately, the other sources in the sample with very high rest-frame $EW(H\alpha)$ are not in the fields with radio data, so we cannot test this further at present.

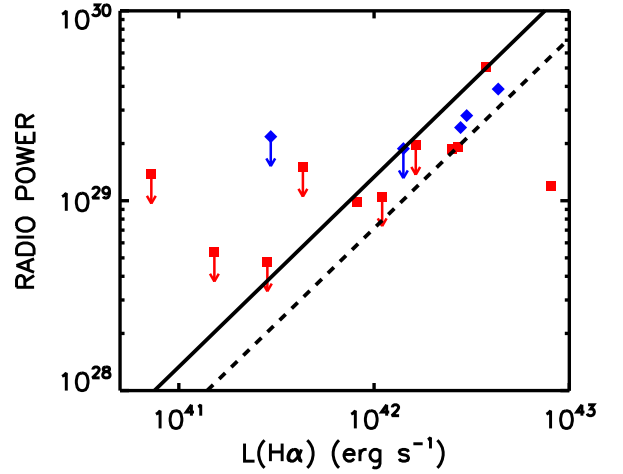


FIG. 19.— The 20 cm power in erg Hz^{-1} vs. the extinction-corrected $H\alpha$ luminosity. The red squares show LAEs, and the blue diamonds show UV-continuum galaxies. In this plot, since we are only testing the star formation rate determinations, we have included sources from the supplement to Table 1 with $EW(Ly\alpha)$ between 15 and 20 \AA . For sources not detected in the 20 cm images we have assumed upper limits of $100 \mu\text{Jy}$ (SIRTF01) and $40 \mu\text{Jy}$ (COSMOS 00). These are shown with downward pointing arrows. The one source in the HDF 00 field is detected at 20 cm. The solid line shows the Condon (1992) SFR vs. radio power relation, and the dashed line shows the Bell (2003) high-luminosity SFR vs. radio power relation.

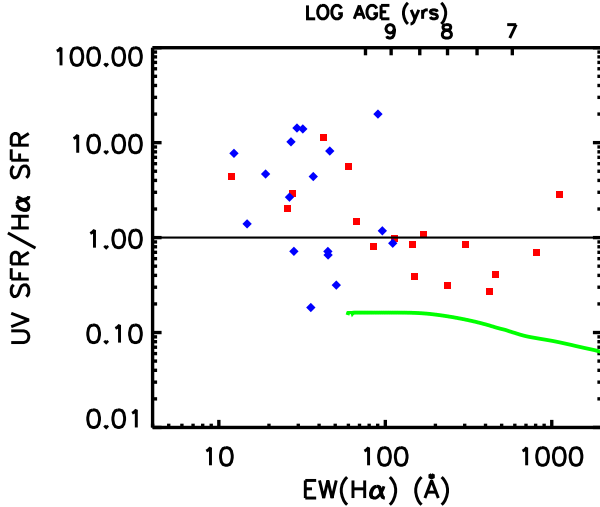


FIG. 20.— The ratio of the SFR computed from the extinction-corrected UV luminosity to that from the extinction-corrected $H\alpha$ luminosity. The red squares show LAEs with $EW(Ly\alpha) \geq 20$ Å, and the blue diamonds show UV-continuum galaxies. In computing the UV SFRs we have applied a small multiplicative offset of 1.17 to scale the NUV *GALEX* spectra to match the NUV *GALEX* magnitudes. The green curve shows the evolution of the 1600 Å F_{λ} for a constant SFR model with a Salpeter (1955) IMF.

SFRs for high-redshift galaxies are generally calculated from the observed UV luminosity together with the stellar extinction correction determined from the UV continuum slope (Meurer et al. 1999). It is therefore interesting to compare the SFRs derived using this method with those computed from the $H\alpha$ luminosities in the present low redshift sample and to estimate the limits of its validity. In Figure 20 we show the ratio of the SFR derived from the stellar extinction corrected UV luminosity with that computed from the nebular extinction corrected $H\alpha$ luminosity as a function of $EW(H\alpha)$. We have computed the UV SFR from the L_{1600} luminosity, extinction corrected using the value derived from the UV spectral index, and converted using the value at $t = 10^8$ yr computed from the STARBURST99 model,

$$\log \text{SFR} = -39.87 + \log L_{1600}. \quad (3)$$

With this calibration the UV SFRs are closely matched to the $H\alpha$ SFRs with an average ratio of 0.9 for sources with $EW(H\alpha) = 60 - 200$ Å. This small absolute difference may be a simple consequence of the relative optical and UV calibrations. As can be seen in Figure 20, the UV calibration underestimates the SFR at higher $EW(H\alpha)$ and overestimates it at lower $EW(H\alpha)$.

The reasons for the deviations reflect the limit of validity of the underlying assumptions. At low $EW(H\alpha)$ the derivation of the UV continuum extinction from the UV spectral slope breaks down. The Meurer et al. (1999) correction is only applicable to starbursting galaxies, since it depends on the intrinsic spectral index being approximately fixed, as is the case for these sources (see Figure 9(c)). At low $EW(H\alpha)$ (less than about 60 Å) the intrinsic UV spectral indices are shallower, and the inappropriate use of the relationship overestimates the SFR, as can be seen in Figure 20. A second problem with the UV continuum method is that the UV continuum flux evolves with time, even in the constant SFR models. In Figure 20

we show (green curve) the evolution of L_{λ} evaluated at 1600 Å (L_{1600}) as a function of $EW(H\alpha)$. (The normalization is arbitrary and depends on the SFR.) The UV luminosity increases as a function of age up to $\sim 10^8$ yr or an $EW(H\alpha) \sim 200$ Å. Thus, the UV continuum calculation combined with the UV spectral index extinction correction should only be used over the $EW(H\alpha) = 60 - 200$ Å range, or, equivalently, for rest-frame line-corrected galaxy colors of $u' - z' = 0.5 - 1.4$ (Figure 9(a)).

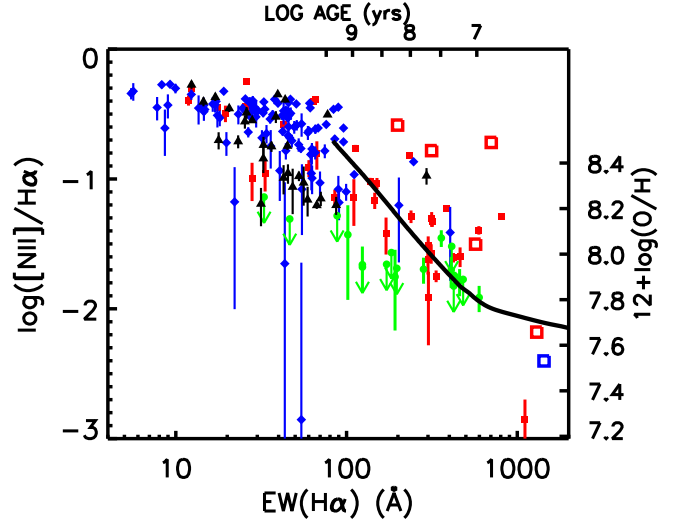


FIG. 21.— Metallicity vs. $EW(H\alpha)$. In addition to the present data points (i.e., Figure 9(f)), we show the blue compact galaxies from Östlin et al. (2009) (open squares: red with $Ly\alpha$ emission, blue without), a continuum-selected sample with $NUV = 22 - 23.25$ from the GOODS-N observations of Barger et al. (2008) with $z = 0.195 - 0.44$ (black triangles), and the ultra-strong $H\alpha$ emission-line selected sample from Hu et al. (2010) (green circles). The error bars are $\pm 1\sigma$, with undetected sources shown with downward pointing arrows at the 1σ level. The black curve shows the model fit discussed in the text. The values of $12 + \log(O/H)$ shown on the right vertical axis were calculated using the Pettini & Pagel (2004) relation.

In Figure 21 we plot the metallicities of the LAE (red solid squares) and UV-continuum (blue diamonds) samples versus the $EW(H\alpha)$. If the gas reservoir were fixed, the constant SFR model would predict that the metallicities should rise linearly with time in the early stages. This is clearly much steeper than is seen in the present samples, which can be approximated by a model where the metallicity rises as $t^{0.3}$ (black curve: this is only shown over the range of validity of the N2 diagnostic which is only appropriate for low metallicity and saturates at near solar metallicity). Thus, the galaxies must have ongoing accretion of gas.

In Figure 21 we also compare the present samples with a fainter continuum sample from the GOODS-N observations of Barger et al. (2008) (black triangles) and with a fainter sample selected to have very high $EW(H\alpha)$ from Hu et al. (2010) (green circles), as well as with the local blue compact galaxy sample of Östlin et al. (2009) (open squares). As might be expected, the fainter samples have systematically lower metallicities than the present data. However, the effect is small compared to the $EW(H\alpha)$ dependence, suggesting that the ages of the galaxies primarily determine the metallicities.

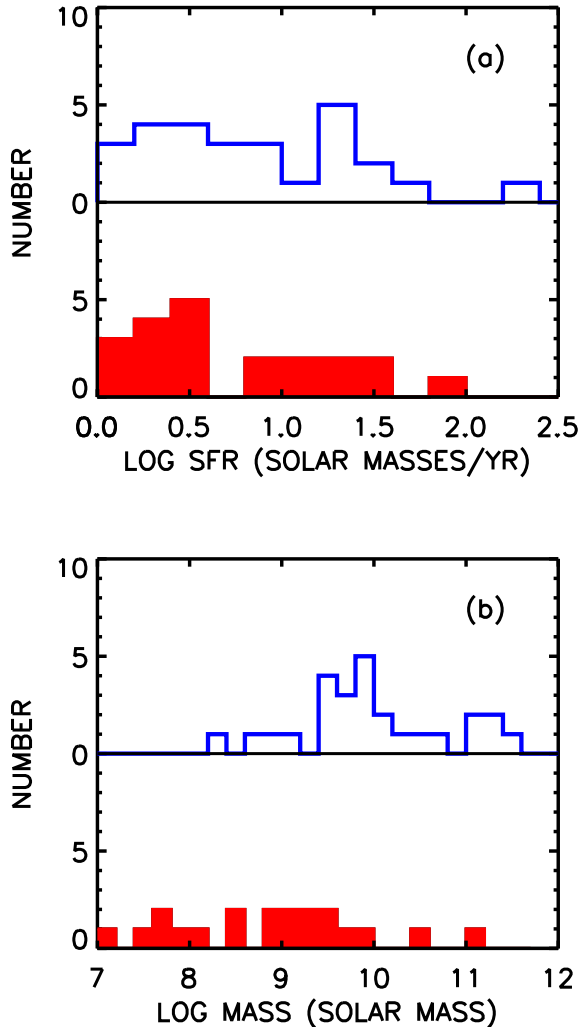


FIG. 22.— (a) The distribution of the SFRs in the LAE (red shaded histogram) and UV-continuum (blue histogram) samples. (b) The distributions of the stellar masses.

Using the SFRs derived from the extinction-corrected $H\alpha$ luminosities and the masses derived from the constant SFR fits to the line-corrected SEDs, we show our final result in Figure 22. In Figure 22(a) we show the distribution of the SFRs. The two samples are nearly identical with a median of $\sim 6 M_{\odot} \text{ yr}^{-1}$. In contrast, as is shown in Figure 22(b), the LAEs, reflecting their younger ages, are systematically lower in mass than the UV-continuum sources. The median mass for the LAEs is $10^9 M_{\odot}$, while that for the UV-continuum sample is $8 \times 10^9 M_{\odot}$.

7. SUMMARY

We analyzed a substantial sample of UV continuum-selected galaxies with and without $\text{Ly}\alpha$ emission lines to try to understand how LAEs are drawn from the general population and how they evolve with redshift. To do this, we obtained extensive optical spectroscopy of *GALEX* grism selected samples (both LAE samples and comparison samples with the same UV magnitude distributions but no detected $\text{Ly}\alpha$) in two redshift intervals: $z = 0.195 - 0.44$ and $z = 0.65 - 1.25$. We used the optical spectroscopy to eliminate AGNs and to obtain the optical

emission-line properties of the samples.

We confirmed that the *GALEX* selected $z \sim 0.3$ LAEs are considerably fainter and much rarer than the high-redshift LAEs (Deharveng et al. 2008; Cowie et al. 2010). Cowie et al. (2010) showed that the L_{\star} in a Schechter (1976) function fit to the $z = 0.195 - 0.44$ LAE luminosity function is almost an order of magnitude fainter than the L_{\star} in a fit at $z \sim 3$ and that only about 5% of $z \sim 0.3$ UV-continuum selected galaxies have rest-frame $\text{EW}(\text{Ly}\alpha) \geq 20 \text{ \AA}$. Here we showed that there are also LAEs that can be found in the *GALEX* spectra at $z \sim 1$ and that these are similar in luminosity to the most luminous high-redshift galaxies. Thus, we conclude that most of the observed evolution occurs over the redshift interval $z = 0 - 1$. This appears to be a simple downsizing effect, with the presence of the higher $\text{Ly}\alpha$ luminosity sources at $z = 1$ corresponding to higher SFR sources initiating their star formation at this redshift.

We showed that at $z = 0.195 - 0.44$, SED fits to strong emission-line galaxies significantly overestimate the ages and masses and underestimate the extinctions if we do not correct for the emission-lines. We found that the SED fits to the uncorrected broadband fluxes give ages of about a Gyr. However, the inferred ages drop substantially when we correct the galaxy broadband magnitudes using the observed spectra to remove the emission-line contributions. All the galaxies with ages much less than a Gyr have strong emission lines and must be corrected for the line contributions. Spectral synthesis fitting shows a smooth evolution of the rest-frame $\text{EW}(H\alpha)$ with age when the emission-line contributions are removed from the broadband fluxes.

We found that at $z = 0.195 - 0.44$, all sources, regardless of the strength of the $\text{Ly}\alpha$ emission line, follow a single, well-defined sequence as a function of the rest-frame $\text{EW}(H\alpha)$. Higher $\text{EW}(H\alpha)$ sources all have lower metallicities, bluer colors, smaller sizes, and less extinction. The number distribution of galaxies versus the $\text{EW}(H\alpha)$ is consistent with a constant formation rate of new galaxies. The bulk ($75 \pm 12\%$) of the LAEs lie at high $\text{EW}(H\alpha) > 100 \text{ \AA}$, and $31 \pm 11\%$ of all UV-continuum selected galaxies with $\text{EW}(H\alpha) > 100 \text{ \AA}$ are LAEs. We conclude that the low-redshift LAEs are primarily drawn from a population of young galaxies that have recently initiated star formation.

It appears that LAEs represent an early stage in a starburst when the star-forming gas is still relatively pristine and the primary star-forming region is small. It also appears that there is a time sequence, with the $\text{Ly}\alpha$ emission line dying away and the metallicity of the gas rising as the galaxy evolves.

We are indebted to the staff of the Keck observatory for their excellent assistance with the observations. We would like to thank Toni Songaila and the anonymous referee for their critical reading of the paper and useful suggestions for improving it. We gratefully acknowledge support from NSF grants AST-0709356 (L. L. C.), AST-0708793 (A. J. B.), and AST-0687850 (E. M. H.), from the University of Wisconsin Research Committee with funds granted by the Wisconsin Alumni Research Foundation and from the David and Lucile Packard Foundation (A. J. B.), and from a NASA grant through an award issued by JPL 1289080 (E. M. H.).

REFERENCES

- Adelman-McCarthy, J. K., et al. 2008, *ApJS*, 175, 297
- Arnouts, S., et al. 2005, *ApJ*, 619, L43
- Atek, H., Kunth, D., Hayes, M., Östlin, G., Mas-Hesse, J. M. 2008, *A&A*, 488, 491
- Atek, H., Kunth, D., Schaerer, D., Hayes, M., Deharveng, J. M., Östlin, G., & Mas-Hesse, J. M. 2009a, *A&A*, 506, L1
- Atek, H., Schaerer, D., & Kunth, D. 2009b, *A&A*, 502, 791
- Balestra, L., et al. 2010, *A&A*, 512, 12
- Baldwin, J. A., Phillips, M. M., & Terlevich, R. 1981, *PASP*, 93, 5 (BPT)
- Bell, E. F. 2003, *ApJ*, 586, 794
- Barger, A. J., & Cowie, L. L. 2010, *ApJ*, 718, 1235
- Barger, A. J., Cowie, L. L., & Wang, W.-H. 2008, *ApJ*, 689, 687
- Bond, N. A., Feldmeier, J. J., Matković, A., Gronwall, C., Ciardullo, R., & Gawiser, E. 2010, *ApJ*, 716, L200
- Bond, N. A., Gawiser, E., Gronwall, C., Ciardullo, R., Altmann, M., & Schawinski, K. 2009, *ApJ*, 705, 639
- Brocklehurst, M. 1971, *MNRAS*, 153, 471
- Bruzual, G., & Charlot, S. 2003, *MNRAS*, 344, 1000
- Calzetti, D., et al. 2000, *ApJ*, 533, 682
- Calzetti, D., Kinney, A. L., & Storchi-Bergmann, T. 1994, *ApJ*, 429, 582
- Cardelli, J. A., Clayton, G. C., & Mathis, J. S. 1989, *ApJ*, 345, 245
- Chapman, S. C., Blain, A. W., Smail, I., & Ivison, R. 2005, *ApJ*, 622, 772
- Charlot, S., & Fall, S. M. 1993, *ApJ*, 415, 580
- Condon, J. J., 1992, *ARA&A*, 30, 575
- Condon, J. J., Cotton, W. D., Helou, G., Shupe, D. L., Soifer, B. T., Storrie-Lombardi, L. J., & Werner, W. M. 2003, *AJ*, 125, 2411
- Cowie, L. L., & Barger, A. J. 2008, *ApJ*, 686, 72
- Cowie, L. L., Barger, A. J., & Hu, E. M. 2010, *ApJ*, 711, 928
- Cowie, L. L., Hu, E. M., & Songaila, A. 2011, *ApJ*, submitted
- Cowie, L. L., Songaila, A., Hu, E. M., & Cohen, J. G. 1996, *AJ*, 112, 839
- Davis, M. et al. 2007, *ApJ*, 660, L1
- Deharveng, J.-M. et al. 2008, *ApJ*, 680, 1072
- Faber, S. M. et al. 2003, *Proc. SPIE*, 4841, 1657
- Felten, J. E. 1976, *ApJ*, 207, 700
- Finkelstein, S. L., Rhoads, J. E., Malhotra, S., Pirzkal, N., & Wang, J. 2007, *ApJ*, 660, 1023
- Finkelstein, S. L., Cohen, S. H., Malhotra, S., Rhoads, J. E., & Papovich, C. 2009a, *ApJ*, 700, 276
- Finkelstein, S. L., Cohen, S. H., Malhotra, S., Rhoads, J. E., Papovich, C., Zheng, Z. Y., & Wang, J.-X. 2009b, *ApJ*, 703, L162
- Finkelstein, S. L., Rhoads, J. E., Malhotra, S., & Grogan, N. 2009c, *ApJ*, 691, 465
- Fitzpatrick, E. L. 1999, *PASP*, 111, 63
- Gawiser, E., et al. 2007, *ApJ*, 671, 278
- Gronwall, C., et al. 2007, *ApJ*, 667, 79
- Hayes, M., et al. 2010, *Nature*, 464, 562
- Hu, E. M., Cowie, L. L., Barger, A. J., Capak, P., Kakazu, Y., & Trouille, L. 2010, *ApJ*, 725, 394
- Hu, E. M., Cowie, L. L., Kakazu, Y., & Barger, A. J. 2009, *ApJ*, 698, 2014
- Hu, E. M., Cowie, L. L., & McMahon, R. G. 1998, *ApJ*, 502, L99
- Izotov, Y. I., Stasińska, G., Meynet, G., Guseva, N. G., & Thuan, T. X. 2006, *A&A*, 448, 955
- Kauffmann, G., et al. 2003, *MNRAS*, 346, 1055
- Kennicutt, R. C. 1998, *ARA&A*, 36, 189
- Kewley, L. J., Dopita, M. A., Sutherland, R. S., Heisler, C. A., & Trewen, J. 2001, *ApJ*, 556, 121
- Kornei, K. A., Shapley, A. E., Erb, D. K., Steidel, C. C., Reddy, N. A., Pettini, M., & Bogosavljević, M. 2010, *ApJ*, 711, 693
- Kunth, D., Leitherer, C., Mas-Hesse, J. M., Östlin, G., & Petrosian, A. 2003, *ApJ*, 597, 263
- Lai, K., et al. 2008, *ApJ*, 674, 70
- Lehmer, B. D., et al. 2005, *ApJS*, 161, 21
- Leitherer, C., et al. 1999, *ApJS*, 123, 3
- Markwardt, C. B. 2009, *ASP Conf. Ser.*, 411, eds. D. Bohlender, P. Dowler, & D. Durand, p.251
- Martin, D. C., et al. 2005, *ApJ*, 619, L1
- Mas-Hesse, J. M., Kunth, D., Tenorio-Tagle, G., Leitherer, C., Terlevich, R. J., & Terlevich, E. 2003, *ApJ*, 598, 858
- Meurer, G., Heckman, T., & Calzetti, D. 1999, *ApJ*, 521, 64
- Morrissey, P., et al. 2007, *ApJS*, 173, 682
- Morrison, G. E., Owen, F. N., Dickinson, M., Ivison, R. J., & Ibar, E. 2010, *ApJS*, 188, 178
- Neufeld, D. A. 1991, *ApJ*, 370, L85
- Nilsson, K. K., et al. 2007, *A&A*, 471, 71
- Nilsson, K. K., & Møller, P. 2009, *A&A*, 508, L21
- Östlin, G., Hayes, M., Kunth, D., Mas-Hesse, J., Leitherer, C., Petrosian, A., & Atek, H. 2009, *AJ*, 138, 923
- Ouchi, M., et al. 2008, *ApJS*, 176, 301
- Overzier, R. A., et al. 2008, *ApJ*, 677, 37
- Pettini, M., & Pagel, B. E. J. 2004, *MNRAS*, 348, L59
- Pilyugin, L. S., & Thuan, T. X. 2005, *ApJ*, 631, 231
- Reddy, N., Erb, D., Pettini, M., Steidel, C. C., & Shapley, A. 2010, *ApJ*, 71, 1070
- Rix, H.-W., et al. 2004, *ApJS*, 152, 163
- Salpeter, E. E. 1955, *ApJ*, 121, 161
- Scarlata, C., et al. 2009, *ApJ*, 704, L98
- Schaerer, D., & deBarros, S. 2009, *A&A*, 502, 423
- Schaerer, D., & Verhamme, A. 2008, *A&A*, 480, 369
- Schechter, P. 1976, *ApJ*, 203, 297
- Schinnerer, E., et al. 2007, *ApJS*, 172, 46S
- Seaton, M. J. 1975, *MNRAS*, 170, 475
- Shapley, A. E., Steidel, C. C., Adelberger, K. L., Dickinson, M., Giavalisco, M., & Pettini, M. 2001, *ApJ*, 562, 95
- Shapley, A. E., Steidel, C. C., Pettini, M., & Adelberger, K. L. 2003, *ApJ*, 588, 65
- Shimasaku, K., et al. 2006, *PASJ*, 58, 313
- Stark, D. P., Ellis, R. S., Chiu, K., Ouchi, M., & Bunker, A. 2010, *MNRAS*, 408, 1628
- Vanzella, E., et al. 2008, *A&A*, 478, 83

APPENDIX

APPENDIX

Since the analysis of Cowie et al. (2010), much deeper *GALEX* grism spectroscopic observations were released for the CDFS 00 field. We have obtained the one- and two-dimensional *GALEX* spectra from MAST and analyzed them to search for Ly α emission using the same procedures as in Cowie et al. (2010). We find a sample of 100 Ly α selected sources within a 32.5 radius field. We give the properties of this sample in Table A1. For each source we give the number, the *GALEX* name, the J2000 right ascension and declination in decimal degrees, the NUV and FUV magnitudes, the redshift inferred from the Ly α emission line in the *GALEX* UV spectrum, the line width in km s $^{-1}$ together with the 1σ error, whether the galaxy is classified as an AGN based on the presence of high-excitation lines in the UV spectrum, and, finally, the optical redshift, if available. The optical redshifts are primarily taken from our DEIMOS spectroscopy, but we also include redshifts from Balestra et al. (2010) and Vanzella et al. (2008), which we note with a colon after the redshift. Where a source lies within the X-ray observations of the Extended Chandra Deep Field-South (ECDF-S) and is (is not) detected in X-rays (Lehmer et al. 2005), we give the logarithm of the rest-frame 2 – 8 keV luminosity (an “E”) in parentheses in the optical redshift column (col. 10).

TABLE A1
GALEX SPECTRAL SAMPLE IDENTIFICATIONS: CDFS 00

Number	Name	R.A. (J2000.0)	Decl. (J2000.0)	NUV	FUV	z_{galax}	Line Width (km/s)	UV class	z_{opt}
(1)	(2)	(3)	(4)	(5)	(6)	(7)	(8)	(9)	(10)
1	GALEX0330-2801	52.550297	-28.028778	21.80	22.33	0.248	1631 \pm 101
2	GALEX0330-2801	52.551250	-28.025417	21.92	22.22	0.248	1714 \pm 90
3	GALEX0330-2748	52.558125	-27.801193	19.64	19.62	0.412	5275 \pm 166
4	GALEX0330-2744	52.574123	-27.741528	21.81	22.55	0.262	2905 \pm 180
5	GALEX0330-2748	52.624916	-27.815805	21.21	23.94	0.855	6278 \pm 133
6	GALEX0330-2803	52.646168	-28.060139	20.04	20.63	0.397	4022 \pm 342
7	GALEX0330-2744	52.665871	-27.747917	21.32	21.96	0.710	7697 \pm 271	AGN	...
8	GALEX0330-2735	52.676125	-27.585638	21.10	22.43	1.130	9441 \pm 173	AGN	...
9	GALEX0330-2759	52.696667	-27.988028	21.15	22.23	0.685	9790 \pm 241	AGN	...
10	GALEX0330-2804	52.732166	-28.067055	19.64	19.93	0.297	3962 \pm 186
11	GALEX0330-2816	52.737499	-28.279444	21.11	21.55	0.281	1940 \pm 73	...	0.2813
12	GALEX0331-2751	52.754875	-27.856834	19.85	21.60	1.186	7273 \pm 153
13	GALEX0331-2742	52.755127	-27.715334	21.24	21.63	0.314	1904 \pm 96
14	GALEX0331-2751	52.760120	-27.858473	21.50	21.97	0.335	3164 \pm 140	...	0.3348
15	GALEX0331-2737	52.765331	-27.621777	21.63	23.62	0.680	2399 \pm 152	...	0.6740
16	GALEX0331-2740	52.790379	-27.666723	21.63	22.54	0.855	10847 \pm 502	AGN	...
17	GALEX0331-2752	52.797752	-27.882500	20.62	21.24	0.264	2426 \pm 115	...	0.2645 (E)
18	GALEX0331-2748	52.800335	-27.800335	22.00	22.37	0.259	2043 \pm 166	...	0.2581 (E)
19	GALEX0331-2755	52.812836	-27.921888	21.96	-999.00	1.011	2969 \pm 212	AGN	1.368 (43.9)
20	GALEX0331-2756	52.836498	-27.946945	21.30	22.24	0.685	8324 \pm 269	AGN	... (43.3)
21	GALEX0331-2816	52.849754	-28.271973	20.92	21.02	0.219	4798 \pm 81	AGN	...
22	GALEX0331-2753	52.850460	-27.894693	21.14	22.03	0.259	2064 \pm 152	...	star (E)
23	GALEX0331-2754	52.854668	-27.916639	21.24	25.93	0.842	2372 \pm 98	...	0.8425 (E)
24	GALEX0331-2818	52.862835	-28.302807	21.71	22.34	0.285	3615 \pm 77	AGN	...
25	GALEX0331-2817	52.869667	-28.283443	21.69	22.06	0.216	2337 \pm 206
26	GALEX0331-2816	52.888245	-28.268251	21.58	21.90	0.219	1814 \pm 152
27	GALEX0331-2820	52.897709	-28.345751	21.95	22.24	0.265	2119 \pm 149
28	GALEX0331-2811	52.930000	-28.196028	21.98	22.22	0.245	1247 \pm 96
29	GALEX0331-2724	52.949291	-27.402834	21.06	22.05	0.369	1887 \pm 219
30	GALEX0331-2811	52.962204	-28.188999	20.68	21.02	0.213	1761 \pm 43	...	0.2129
31	GALEX0331-2814	52.976501	-28.238640	21.49	21.84	0.280	2169 \pm 39	...	0.2804
32	GALEX0331-2814	52.978458	-28.235861	21.26	22.10	0.316	2026 \pm 81	...	0.3164
33	GALEX0331-2809	52.985916	-28.158251	19.56	22.67	1.215	13072 \pm 0	AGN	...
34	GALEX0331-2809	52.999332	-28.164444	21.18	21.43	0.236	1482 \pm 50	...	0.2364
35	GALEX0332-2810	53.001919	-28.182611	21.97	22.46	0.280	2798 \pm 133
36	GALEX0332-2809	53.025002	-28.161083	21.79	22.32	0.222	2576 \pm 219
37	GALEX0332-2722	53.045292	-27.378277	21.97	22.15	0.308	2274 \pm 81
38	GALEX0332-2809	53.049374	-28.153194	20.49	21.09	0.239	1928 \pm 133
39	GALEX0332-2801	53.049751	-28.025057	21.51	21.71	0.215	2049 \pm 41	...	0.2155 (E)
40	GALEX0332-2811	53.061584	-28.186527	21.18	21.71	0.265	2193 \pm 85
41	GALEX0332-2813	53.077999	-28.222443	21.17	21.42	0.279	3512 \pm 54	...	0.2787
42	GALEX0332-2744	53.080002	-27.745890	21.51	21.75	0.217	2577 \pm 183	...	0.2169: (E)
43	GALEX0332-2734	53.084042	-27.573084	21.55	-999.00	0.971	2735 \pm 124	...	0.9650 (E)
44	GALEX0332-2758	53.102917	-27.977055	21.50	22.55	0.380	2115 \pm 230 (E)
45	GALEX0332-2741	53.112461	-27.684694	19.82	21.18	0.742	9192 \pm 57	AGN	0.7423: (44.0)
46	GALEX0332-2745	53.125000	-27.758305	21.36	23.93	1.209	9690 \pm 331	AGN	1.209: (43.6)
47	GALEX0332-2745	53.126251	-27.750751	21.63	23.13	0.740	8176 \pm 393	AGN	... (43.1)
48	GALEX0332-2810	53.155334	-28.177500	21.01	21.32	0.204	2778 \pm 143	...	0.2035
49	GALEX0332-2808	53.155956	-28.146500	20.81	22.03	0.775	8628 \pm 216	AGN	...
50	GALEX0332-2739	53.158794	-27.662472	20.88	22.03	0.838	6950 \pm 65	AGN	0.8376: (43.5)

TABLE A1 (CONT)
GALEX SPECTRAL SAMPLE IDENTIFICATIONS: CDFS 00

Number	Name	R.A. (J2000.0)	Decl. (J2000.0)	NUV	FUV	z_{galax}	Line Width (km/s)	UV class	z_{opt}
(1)	(2)	(3)	(4)	(5)	(6)	(7)	(8)	(9)	(10)
51	GALEX0332-2746	53.162796	-27.767221	21.94	-999.00	1.216	3491± 152	...	1.216 (43.3)
52	GALEX0332-2811	53.174255	-28.190306	20.27	20.17	0.204	2190± 20	...	0.2044
53	GALEX0332-2810	53.184078	-28.174473	21.04	21.83	1.148	7987± 109	AGN	1.148
54	GALEX0332-2822	53.187252	-28.375973	-999.00	23.26	0.795	4410± 243
55	GALEX0332-2822	53.191708	-28.375555	20.32	21.94	0.837	5472± 22	...	0.8375
56	GALEX0332-2747	53.195126	-27.787361	22.12	21.97	0.228	2294± 53	...	0.2266 (E)
57	GALEX0332-2732	53.208038	-27.545000	21.81	21.91	0.219	4546± 235	...	0.2190 (E)
58	GALEX0332-2803	53.213581	-28.051723	21.88	22.30	0.213	3259± 199 (40.9)
59	GALEX0332-2748	53.221958	-27.809139	21.56	21.64	0.227	1913± 21	...	0.2273: (E)
60	GALEX0332-2753	53.236000	-27.887974	20.62	21.10	0.365	2365± 172	...	0.3650: (E)
61	GALEX0332-2757	53.238041	-27.960222	20.48	20.72	0.369	1713± 211 (E)
62	GALEX0332-2823	53.240459	-28.388306	20.83	21.30	0.214	1834± 45	...	0.2137
63	GALEX0333-2821	53.258461	-28.357668	21.08	21.26	0.247	2006± 77	...	0.2472
64	GALEX0333-2813	53.268044	-28.227165	20.88	22.75	1.015	4922± 203
65	GALEX0333-2744	53.280293	-27.742418	20.27	20.79	0.220	2677± 128	...	0.2167 (E)
66	GALEX0333-2820	53.286755	-28.333389	21.49	22.10	0.370	2000± 273
67	GALEX0333-2801	53.301208	-28.022917	21.63	22.33	0.291	2371± 205 (E)
68	GALEX0333-2759	53.333374	-27.986778	21.56	22.19	0.685	9118± 487	AGN	0.6830 (42.9)
69	GALEX0333-2739	53.337746	-27.653334	20.75	21.76	1.235	12112± 309	AGN	1.235 (43.8)
70	GALEX0333-2733	53.340416	-27.560862	21.74	22.18	0.277	1760± 32	...	0.2716 (E)
71	GALEX0333-2725	53.352249	-27.430723	19.64	21.21	1.140	8262± 34	AGN	...
72	GALEX0333-2727	53.359249	-27.454334	21.17	21.61	0.352	3309± 123
73	GALEX0333-2756	53.370708	-27.944500	21.02	22.32	0.840	7874± 87	AGN	0.8410 (44.0)
74	GALEX0333-2759	53.371666	-27.990665	21.66	22.52	0.766	6334± 190	AGN	0.7630 (43.5)
75	GALEX0333-2822	53.386753	-28.372250	20.33	21.65	0.856	7211± 77	AGN	0.8560
76	GALEX0333-2756	53.389545	-27.946222	21.49	22.04	0.429	2658± 163 (E)
77	GALEX0333-2822	53.389584	-28.376223	21.89	22.37	0.305	3233± 252
78	GALEX0333-2817	53.414040	-28.290001	20.10	21.19	0.991	7126± 40	AGN	...
79	GALEX0333-2821	53.448460	-28.364695	20.58	21.40	0.248	4145± 231	...	0.2479
80	GALEX0333-2814	53.471249	-28.248138	-999.00	21.51	0.202	2544± 198
81	GALEX0333-2749	53.489918	-27.819473	21.63	22.08	0.245	1795± 143
82	GALEX0333-2757	53.496414	-27.966471	21.64	22.39	0.363	2685± 126
83	GALEX0334-2756	53.517040	-27.941610	21.02	22.12	0.988	9676± 114	AGN	...
84	GALEX0334-2729	53.524834	-27.490499	20.96	22.01	0.677	8968± 205	AGN	...
85	GALEX0334-2807	53.530334	-28.119139	20.59	22.09	1.080	9276± 144	AGN	...
86	GALEX0334-2754	53.533707	-27.902000	20.92	21.40	0.383	1088± 0
87	GALEX0334-2743	53.534622	-27.727055	20.38	21.36	1.028	7426± 57	AGN	...
88	GALEX0334-2815	53.541294	-28.255499	21.57	22.77	0.337	2479± 209	...	0.3369
89	GALEX0334-2752	53.554749	-27.880083	21.74	21.79	0.236	1971± 100	...	0.2333
90	GALEX0334-2746	53.567707	-27.768970	21.24	21.47	0.380	20979± 0
91	GALEX0334-2745	53.570290	-27.751194	20.19	23.38	1.163	7013± 41	AGN	...
92	GALEX0334-2812	53.581249	-28.211390	21.80	24.04	0.846	5111± 153	AGN	...
93	GALEX0334-2803	53.586754	-28.065695	21.23	22.06	0.360	2027± 154
94	GALEX0334-2737	53.602165	-27.632471	20.43	20.92	0.372	2619± 242
95	GALEX0334-2753	53.623749	-27.893917	21.80	24.35	1.040	3095± 94	...	1.036
96	GALEX0334-2759	53.662498	-27.987583	21.40	22.01	0.870	6663± 184	AGN	...
97	GALEX0334-2743	53.711334	-27.729334	20.86	21.51	0.323	2372± 92
98	GALEX0334-2752	53.711498	-27.876585	21.67	22.00	0.337	2323± 90	...	0.3336
99	GALEX0334-2749	53.721710	-27.824833	20.60	21.40	0.343	3286± 247
100	GALEX0334-2748	53.729584	-27.800833	19.82	20.55	0.314	2272± 53